

REPORT DOCUMENTATION PAGE			Form Approved OMB NO. 0704-0188	
Public Reporting burden for this collection of information is estimated to average 1 hour per response, including the time for reviewing instructions, searching existing data sources, gathering and maintaining the data needed, and completing and reviewing the collection of information. Send comment regarding this burden estimates or any other aspect of this collection of information, including suggestions for reducing this burden, to Washington Headquarters Services, Directorate for Information Operations and Reports, 1215 Jefferson Davis Highway, Suite 1204, Arlington, VA 22202-4302, and to the Office of Management and Budget, Paperwork Reduction Project (0704-0188), Washington, DC 20503.				
1. AGENCY USE ONLY (Leave Blank)		2. REPORT DATE April 15, 2003		3. REPORT TYPE AND DATES COVERED Final Report October 1, 2002- December 31, 2003
4. TITLE AND SUBTITLE Investigation of Ultrafast Condensed Phase Reactions Between Nanopowders			5. FUNDING NUMBERS DAAD 19-02-1-0456	
6. AUTHOR(S) Jan A. Puszynski				
7. PERFORMING ORGANIZATION NAME(S) AND ADDRESS(ES) South Dakota School of Mines and Technology 501 E. St. Joseph Street Rapid City, SD 57701			8. PERFORMING ORGANIZATION REPORT NUMBER 2	
9. SPONSORING / MONITORING AGENCY NAME(S) AND ADDRESS(ES) U. S. Army Research Office P.O. Box 12211 Research Triangle Park, NC 27709-2211			10. SPONSORING / MONITORING AGENCY REPORT NUMBER 44550.1-EG	
11. SUPPLEMENTARY NOTES The views, opinions and/or findings contained in this report are those of the author(s) and should not be construed as an official Department of the Army position, policy or decision, unless so designated by other documentation.				
12 a. DISTRIBUTION / AVAILABILITY STATEMENT Approved for public release; distribution unlimited.			12 b. DISTRIBUTION CODE	
13. ABSTRACT (Maximum 200 words) The specific research objectives of this grant were on mathematical modeling of ultrafast condensed phase reactions with and without pressure gradients generated by the reaction and on investigation of combustion characteristics of reacting systems consisting of nanopowders. One-dimensional mathematical models were derived and solved numerically. These models predict qualitatively combustion front propagation in such reacting systems. It was also found that surface functionalization of aluminum nanopowders significantly slows down its reaction with moisture. It was demonstrated experimentally that coated aluminum nanopowders with oleic acid or silanes react even better with copper, molybdenum, and tungsten oxides. This interesting discovery can be explained by more ultimate mixing of heterogeneous reactants. In addition, results on characterization of nanopowders and mixing of nanoreactants are presented as well.				
14. SUBJECT TERMS nanoenergetic materials, metastable intermolecular composites, mathematical modeling			15. NUMBER OF PAGES 54	
			16. PRICE CODE	
17. SECURITY CLASSIFICATION OR REPORT UNCLASSIFIED	18. SECURITY CLASSIFICATION ON THIS PAGE UNCLASSIFIED	19. SECURITY CLASSIFICATION OF ABSTRACT UNCLASSIFIED	20. LIMITATION OF ABSTRACT UL	

NSN 7540-01-280-5500

Standard Form 298 (Rev.2-89)
Prescribed by ANSI Std. Z39-18
298-102

FINAL REPORT

INVESTIGATION OF ULTRAFAST CONDENSED PHASE REACTIONS BETWEEN NANOPOWDERS

Prepared By:

**Dr. Jan A. Puszynski
South Dakota School of Mines and Technology
501 E. St. Joseph Street
Rapid City, SD 57701
Tel: 605/394-5268
Fax: 605/394-5265
E-mail: Jan.Puszynski@sdsmt.edu**

**This material is based upon work supported by the U.S. Army Research Office under the
grant number DAAD19-02-1-0456**

May 2004

TABLE OF CONTENTS

FOREWORD.....	1
LIST OF FIGURES.....	1
LIST OF TABLES.....	4
STATEMENT OF THE PROBLEM STUDIED.....	5
SUMMARY OF THE MOST IMPORTANT RESULTS.....	5
1. CHARACTERIZATION OF ALUMINUM NANOPOWDERS.....	6
2. AGING STUDIES OF NANOSIZE ALUMINUM POWDERS.....	9
3. MIXING OF NANOSIZE ALUMINUM AND TITANIUM DIOXIDE POWDERS.....	14
4. MEASUREMENTS OF PROPAGATION VELOCITIES.....	20
5. MATHEMATICAL MODELING OF CONDENSED-PHASE COMBUSTION.....	25
BIBLIOGRAPHY.....	50
PUBLICATIONS, PRESENTATIONS, AND TECHNICAL REPORTS.....	51
PARTICIPATING PERSONNEL.....	51
REPORT OF INVENTIONS.....	52

FOREWORD

This sponsored research program closely accompanied research activities of the DURINT grant sponsored by the U.S. Army Research Office. The specific research objectives of this grant were on mathematical modeling of ultrafast condensed phase reactions with and without pressure gradients generated by the reaction and on investigation of combustion characteristics of reacting systems consisting of nanopowders. One-dimensional mathematical models were derived and solved numerically. These models predict qualitatively combustion front propagation in such reacting systems. It was also found that surface functionalization of aluminum nanopowders significantly slows down its reaction with moisture. It was demonstrated experimentally that coated aluminum nanopowders with oleic acid or silanes react even better with copper, molybdenum, and tungsten oxides. This interesting discovery can be explained by more ultimate mixing of heterogeneous reactants. In addition, results on characterization of nanopowders and mixing of nanoreactants are presented as well.

LIST OF FIGURES

Figure 1. TEM image of passivated aluminum nanopowder.

Figure 2. X-ray patterns of passivated aluminum and products of combustion in oxygen (alumina) and in air (alona).

Figure 3. Schematic of the glassware for the determination of the reactive aluminum content by the volumetric method.

Figure 4. Schematic of the stopper used in neck 6. Sample cup is a metal piece bonded to the end of the glass stopper.

Figure 5. Schematic of an aging chamber.

Figure 6. Aging results for uncoated Al (UFAl I-65-38).

Figure 7. Aging results for coated and uncoated Al at 43 %RH.

Figure 8. Aging results for coated and uncoated Al at 75 %RH.

Figure 9. Aging results for coated and uncoated Al at 84 %RH.

Figure 10. Aging results for coated and uncoated Al at 97 %RH.

Figure 11: Results for aging of Nanotechnologies and Technanogy aluminum samples in 97 %RH at 40 °C. Lines shown are trendlines only and each data point is an average of two volumetric method measurements.

Figure 12. Al-TiO₂-mixture prepared in absolute ethanol with sodium dioctyl sulfosuccinate as surfactant (SE-image 10000 X).

Figure 13. Al-TiO₂-mixture prepared in absolute ethanol with sodium dioctyl sulfosuccinate as surfactant (BSE-image 10000 X).

Figure 14. Al-TiO₂-mixture prepared in n-hexane with sodium dioctyl sulfosuccinate as surfactant (SE-image 10000 X).

Figure 15. Al-TiO₂-mixture prepared in n-hexane with sodium dioctyl sulfosuccinate as surfactant (BSE-image 10000 X).

Figure 16: Al-TiO₂-mixture prepared in absolute ethanol with sodium dioctyl sulfosuccinate as surfactant (Cameo-image 10000 X).

Figure 17. Al-TiO₂-mixture prepared in n-hexane with sodium dioctyl sulfosuccinate as surfactant (Cameo-image 10000 X).

Figure 18. Al-TiO₂-mixture prepared in absolute ethanol with sodium dioctyl sulfosuccinate as surfactant (Elemental Mapping 10000 X SE-BSE-Al and Ti mapping image).

Figure 19. Al-TiO₂-mixture prepared in n-hexane with sodium dioctyl sulfosuccinate as surfactant (Elemental Mapping 10000 X SE-BSE-Al and Ti mapping image).

Figure 20. Al-TiO₂-mixture prepared in absolute ethanol with sodium dioctyl sulfosuccinate as surfactant (Three line scans of 10 μm at 10000 X).

Figure 21. Al-TiO₂-mixture prepared in n-hexane with sodium dioctyl sulfosuccinate as surfactant (Three line scans of 10 μm at 10000 X).

Figure 22. Al-TiO₂-mixture prepared in absolute ethanol with sodium dioctyl sulfosuccinate as surfactant. Sample after three line scans of 10 μm at 10000X.

Figure 23. Al-TiO₂-mixture prepared in absolute ethanol with sodium dioctyl sulfosuccinate as surfactant. Sample after three line scans of 10 μm at 10000X. The X-ray spot analyses at four points for aluminum and titanium show the following results #1 (Al: 44.7 Ti: 55.3), #2 (Al: 48.4 Ti: 51.6), #3 (Al: 48.8 Ti: 51.2), #4 (Al: 40.8 Ti: 59.2).

Figure 24. Al-TiO₂-mixture prepared in n-hexane with sodium dioctyl sulfosuccinate as surfactant. Sample after the three line-scans of 10 μm at 10000 X.

Figure 25. Images of burning loose nanopowders of Al-MoO₃ system recorded, with

perforated baffles, using high-speed camera.

Figure 26. Results for the measurement of propagation velocity of Al/CuO as a function of weight percent coating on the aluminum nano-powder. The coatings used were Z6124 silane and oleic acid. Each data point is the average of 4 measurements.

Figure 27. Propagation velocity as a function of coating concentration. Coatings were added at the time of mixing of Al/CuO reactants

Figure 28. Al/CuO ignition delay results for coated aluminum sample. Coatings studied were Z6124 Silane and oleic acid.

Figure 29. Schematic of the cylindrical reacting sample.

Figure 30. Tridiagonal matrixes for energy equation (Eq.25).

Figure 31. Screen shoot of window version.

Figure 32. Temperature profile in a non-reacting cylindrical sample with $\Delta\tau = 0.004$.

Figure 33. Temperature profile in the cylindrical sample with $\Delta\tau = 0.004$.

Figure 34. Conversion profile in the cylindrical sample with $\Delta\tau = 0.004$.

Figure 35. Temperature profile in a reacting cylindrical sample for frequency factor of $1.728E10s^{-1}$ with $\Delta\tau = 0.002$.

Figure 37. Temperature profile in the reacting cylindrical sample for frequency factor of $2.016e10s^{-1}$ with $\Delta\tau = 0.002$.

Figure 38. Resulted matrix for energy equation.

Figure 39. Continuity equation matrix.

Figure 40. Dimensionless pressure profile for non-reacting system with $\Delta\tau = 0.005$.

Figure 41. Dimensionless density profile for non-reacting system with $\Delta\tau = 0.005$.

Figure 42. Dimensionless temperature profile for non-reacting system with $\Delta\tau = 0.005$.

Figure 43. Dimensionless pressure profile with $\Delta\tau = 0.005$.

Figure 44. Dimensionless density profile for 50 bars (725 psi) with $\Delta\tau = 0.005$.

Figure 45. Dimensionless temperature profile for 50 bar (725 psi) with $\Delta\tau = 0.005$.

Figure 46. Dimensionless velocity profile for 50 bar (725 psi) with $\Delta\tau = 0.005$.

Figure 47. Conversion profile for 50 bar (725 psi) with $\Delta\tau = 0.005$.

Figure 48. Dimensionless pressure profile with $\Delta\tau = 0.004$.

Figure 49. Dimensionless temperature profile for 70 bars (1000 psi) with $\Delta\tau = 0.004$.

Figure 50. Dimensionless density for 70 bars (1000 psi) with $\Delta\tau = 0.004$.

Figure 51. Dimensionless velocity profile for 70 bars (1000 psi) pressure with $\Delta\tau = 0.004$.

Figure 52. Conversion profile for pressure 70 bars (1000 psi) with $\Delta\tau = 0.004$.

Figure 53. Dimensionless pressure profile with $\Delta\tau = 0.003$.

Figure 54. Dimensionless temperature profile for 2000 psi pressure with $\Delta\tau = 0.003$.

Figure 55. Dimensionless density profile for 2000 psi pressure with $\Delta\tau = 0.003$.

Figure 56. Dimensionless velocity profile for 2000 psi pressure with $\Delta\tau = 0.003$.

Figure 57. Conversion profile for 2000 psi pressure with $\Delta\tau = 0.003$.

Figure 58. Dimensionless velocity profile at various pressures.

LIST OF TABLES

Table 1. TGA analyses of aluminum nanopowders obtained from NSWCI/H.

Table 2. Salt solutions for maintaining humidity.

Table 3. Average propagation velocity of the investigated systems under unconfined conditions.

Table 4. Results for the measurement of propagation velocity of Al/CuO as a function of weight percent coating on the aluminum nano-powder. The coatings used were Z6124 silane and oleic acid.

STATEMENT OF THE PROBLEM STUDIED

Metal-based energetic materials, under certain stimuli, release large amounts of energy. They are essential ingredients in rocket propellants, primers, and warhead explosives. However, rate of energy release for these metal-based energetic materials are rather slow. Metal-based energetic materials that are produced in nano-scale are potentially attractive due to their rapid energy release. This increased performance is due to a significant increase in the specific surface area of all involved reactants. As the specific surface area increases, the number of contact points between the reactants also increases. Review of recent literature on the combustion of pyrotechnic materials has shown that there is a significant relation between reaction rate and particle size. Reducing particle size results in increase of combustion front velocity due to reduced diffusional distances between reactant particles. Further, reaction rate depends on various factors including particle size distribution and degree of intermixing. Reaction rates between nanosize aluminum and metal oxides can be significantly greater than those observed with traditional micron-size thermite powders. One class of nano-scale metal-based energetic materials includes systems consisting of nanosize aluminum and metal oxide as an oxidizer. This type of reacting system is known as metastable intermolecular composite (MIC). In other words, MIC is a mixture of nano-scale energetic constituents exhibiting a thermite behavior. Such reactions occurring between metal and metal oxide powders are accompanied by the generation of high temperatures ($>3000\text{K}$). Super-thermites, formed by combining aluminum and metal oxide nanopowders are currently incorporated in formulating the next generation of environmentally friendly primers and lead-free matches. They may also find an application in air bag initiators and inflators, and thermal batteries. Until now, general combustion characteristics of MIC reacting systems have not been well understood therefore this research study was focused on better understanding of combustion front propagation characteristics using both experimental and theoretical tools. The experimental studies were focused on functionalization of aluminum nanopowder in order to reduce the aging effect of moisture, improve its dispersion in organic solvents, and improve mixing with oxide nanopowders. The effect of aluminum surface modification on aging and reactivity of nanopowders with copper oxide were studied extensively. The experimental research was accompanied by numerical studies of a combustion front propagation in the presence of pressure gradients generated during the reaction.

SUMMARY OF THE MOST IMPORTANT RESULTS

During the first period of research grant October 1, 2002 - December 31, 2003 the following research initiatives have been undertaken:

- Functionalization and characterization of aluminum nanopowders.
- Aging studies of aluminum nanopowders at different relative humidities.
- Investigation of reactivity of aluminum with copper oxide nanopowders under unconfined conditions.
- Effect of coating of aluminum nanopowders on combustion front velocities.
- Mixing studies of systems consisting of binary nanopowders.

- Mathematical model describing combustion front propagation in condensed phase system with and without products vaporization.

1. CHARACTERIZATION OF ALUMINUM NANOPOWDERS

Aluminum is very reactive metal that undergoes quick oxidation and hydration at ambient conditions. Particularly, the nanosize aluminum particles with large exposed surface can react violently with oxygen (nanosize, pure aluminum metal is pyrophoric). Preparation of oxide passivation barrier on the particle's surface controls this process and, frequently, the nanosize aluminum available on the market is an oxide-passivated material.

A typical TEM image of passivated Al nanopowder is shown in Figure 1. As can be seen from that photograph, a thin layer (approximately 1.5-2.5 nm) of aluminum oxide is present on the aluminum surface.

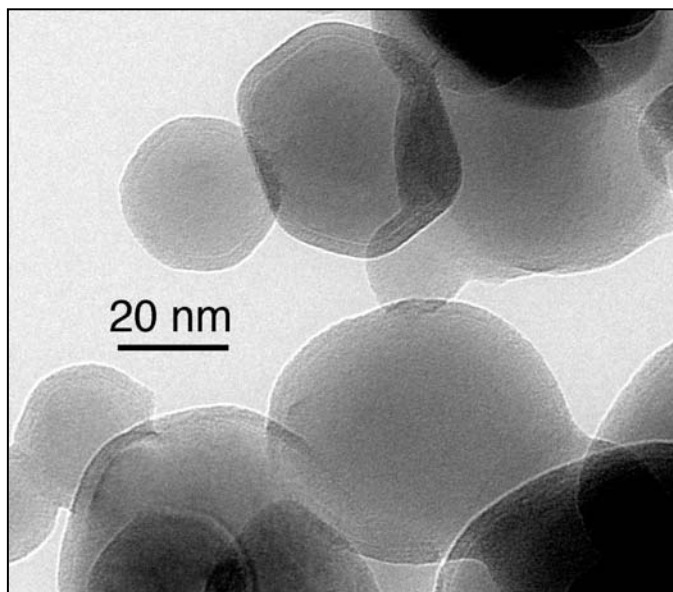


Figure 1. TEM image of passivated aluminum nanopowder.

Even a thin layer of the oxide on the surface amounts for large reduction of the reactive Al content of the passivated material. Quantitative assessment of the active aluminum in the nanopowder is essential for designing and carrying out experiments where stoichiometry of the reactants is relevant. Therefore, our research studies were focused on quantitative determination of the content of reactive aluminum in passivated Al nanopowders. Both, TGA and volumetric method were used in these studies.

The amount of reactive aluminum determined from TGA analyses conducted both in air and oxygen, is apparently lower than expected. A sudden ignition of the aluminum sample leads to the melting of the aluminum within an oxide product. This melting process prevents completion of the oxidation process by entrapping unreacted aluminum inside the macroscopic aluminum oxide droplet. In order to prevent the formation of such droplets in next experiments, submicron alumina powder was used as a diluent. It was determined that approximately 35 mg of

Al_2O_3 was needed to mix with 5 mg of Al nanopowder. It was also determined that an additional 10% weight increase was recorded in TGA experiment as the applied temperature increased from 800 to 1450°C. In order to ascertain the completeness of oxidation, the final experiments were carried out until 1450°C. The results are shown in Table 1.

Table 1. TGA analyses of aluminum nanopowders obtained from NSWC/IH.

Al nanopowder (surface area)	Gas Atmosphere	Average % of Reactive Aluminum Content Temperature: 25-1450 °C
1030001 – (34.5 m ² /g)	Air	68
1-65-38 – (79.1 m ² /g)	Air	48
1-62-37 – (50.3 m ² /g)	Air	67

Another important factor affecting TGA analysis of Al nanopowders is the choice of a reactive gas. Normally, air is used in most combustion experiments. However, it was determined in our experiments these research studies that the product of combustion of aluminum in air is not pure aluminum oxide but solid solution of that oxide with aluminum nitride. The latter component is the product of reaction of aluminum with nitrogen in air. The material obtained from combustion in air is alon (trace 3 in Figure 2).

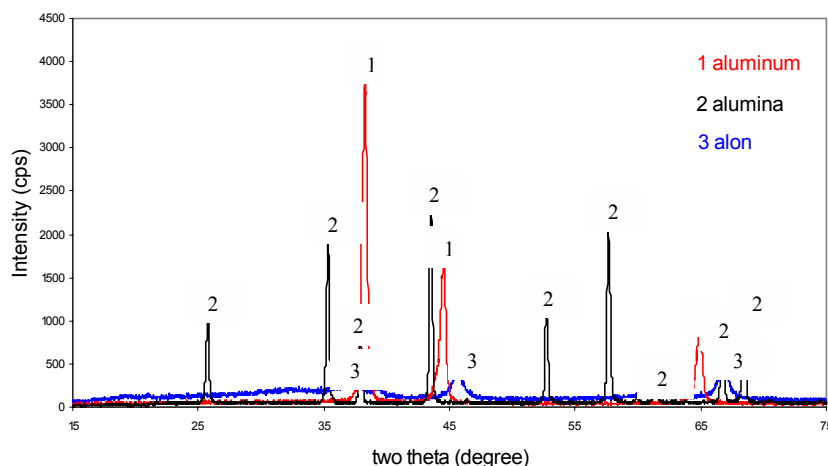
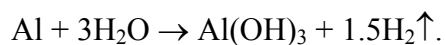


Figure 2. X-ray patterns of passivated aluminum and products of combustion in oxygen (alumina) and in air (alon).

The TGA technique is not very suitable for measurement of reactive aluminum content in polymer coated Al nanopowders due to simultaneous oxidation of metal and polymer. Therefore, another method based on wet chemistry (volumetric method) is more suitable in such situations. The volumetric method used in this research for characterization of nanosized aluminum powder was also revised to introduce improvements in accuracy and convenience. The principle concept of this method is a selective reaction between aluminum powder and water in the presence of sodium hydroxide (NaOH):



By measuring volume of generated hydrogen one can infer about amount of equivalent aluminum involved in the reaction. In calculations the precise determination of ambient pressure and temperature is required. Saturation with water of nitrogen gas used for purging the apparatus is also needed to minimize experimental errors.

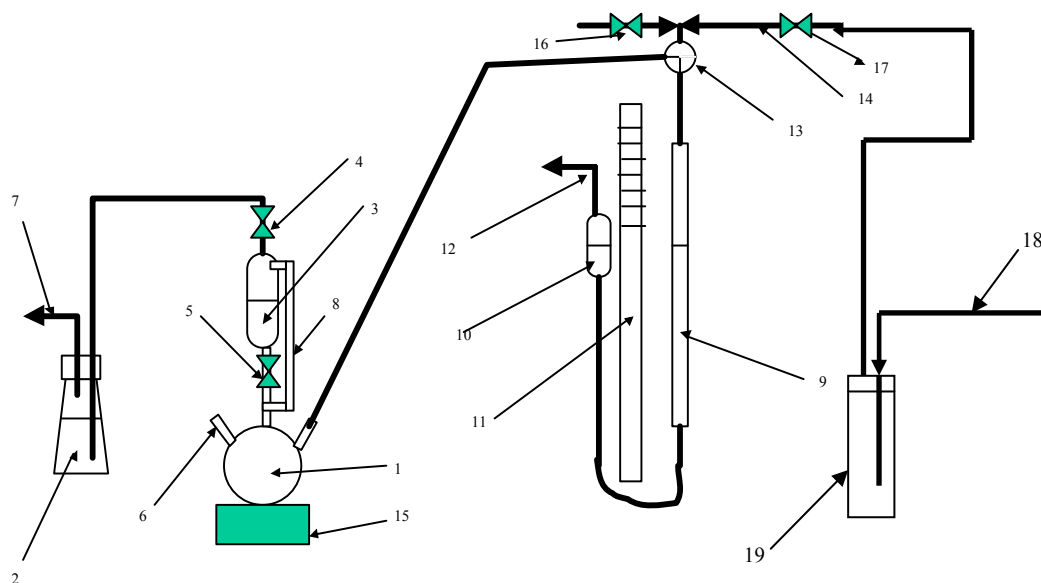


Figure 3. Schematic of the glassware for the determination of the reactive aluminum content by the volumetric method.

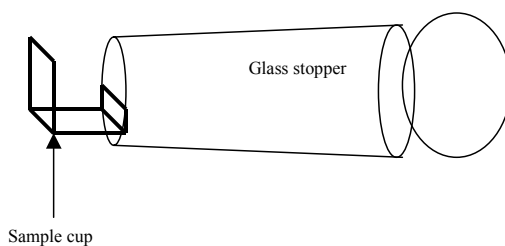


Figure 4. Schematic of the stopper used in neck 6. Sample cup is a metal piece bonded to the end of the glass stopper.

The experimental procedure was described in detail in the previous progress report.

5. AGING STUDIES OF NANOSIZE ALUMINUM POWDERS.

A systematic study of slow oxidation of aluminum nanopowders in presence of various partial pressure of water was undertaken to develop effective measures for preventing aging of the nanopowder in ambient conditions.

Sample vials containing untreated (as received) aluminum, UFAL 1-65-38, were placed in sealed vessels maintaining relative humidity of 43, 75, 83, and 97 percent. The sample vials were open to the vessel atmosphere. The vessels were placed in an oven maintained at 40°C. See Figure 5 below for a schematic of the humidity vessel.

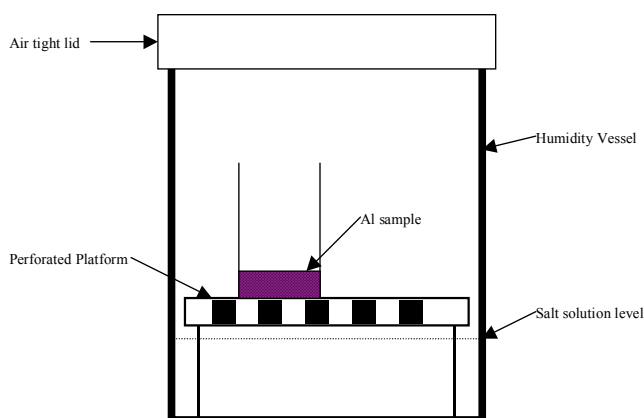


Figure 5. Schematic of an aging chamber.

The relative humidity (RH) inside each vessel was maintained with selected saturated aqueous salt solutions as recommended in ASTM Standard E 104-85 *Standard Practice for Maintaining Constant Relative Humidity by Means of Aqueous Solutions*. The aqueous salt solutions used were potassium carbonate, sodium chloride, potassium chloride, and potassium sulfate. See Table 2 below for the salt solutions and their %RH.

Table 2. Salt solutions for maintaining humidity.

K ₂ CO ₃	NaCl	KCl	K ₂ SO ₄
43%RH	75%RH	83%RH	97%RH

Samples of the aged powders were tested for percent reactive Al using the volumetric method. Samples were taken approximately every 3 or 6 days depending on the humidity the sample is exposed to. The results are shown in Figure 6.

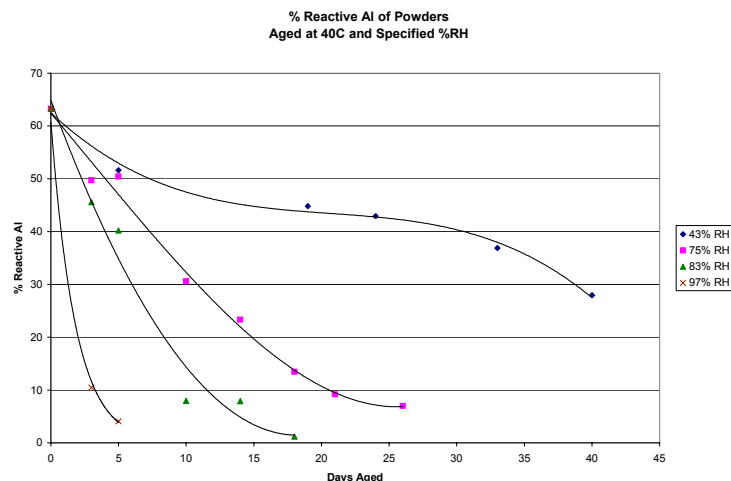


Figure 6. Aging results for uncoated Al (UFAl 1-65-38).

Untreated aluminum nanopowder exposed to humid air undergoes oxidation, particularly rapidly at humid conditions. This process leads to drastic reduction of the reactive aluminum content. In order to prevent or effectively slow down deterioration of the material, application of various surface coatings were considered.

Aluminum nanopowder coating experiments are currently underway utilizing several Dow Corning silanes. Two samples of UFAl 1-65-38 aluminum have been dispersed with 3 wt% silane. The silanes currently being examined are Dow Corning Z-6124 and Z-6040. The coated Al samples were aged under the same conditions as the above aging experiment to determine their effectiveness. An uncoated aluminum sample was aged concurrently with the coated samples as a control. The coating procedure is as follows:

Coating Procedure:

1. Al sample is weighed out and placed in a vial.
2. The required weight of silane is added to the vial. The silane is contained in a previously prepared stock solution, of silane and methanol, of known silane concentration. A calculated weight of stock solution is weighed into the vial.
3. Methanol is used to dilute/disperse the Al and silane in the vial.
4. The vial is seal and sonicated for 15 minutes.
5. After sonication the dispersed Al/silane/methanol solution is poured into a pan and the methanol allowed to evaporate leaving behind the Al and silane.
6. The Al/silane powder is then collected from the pan.

Results for the aging of Al coated with 3 wt.% Dow Corning Z-6124 and Z-6040 silane and uncoated Al are shown in Figures 7-10.

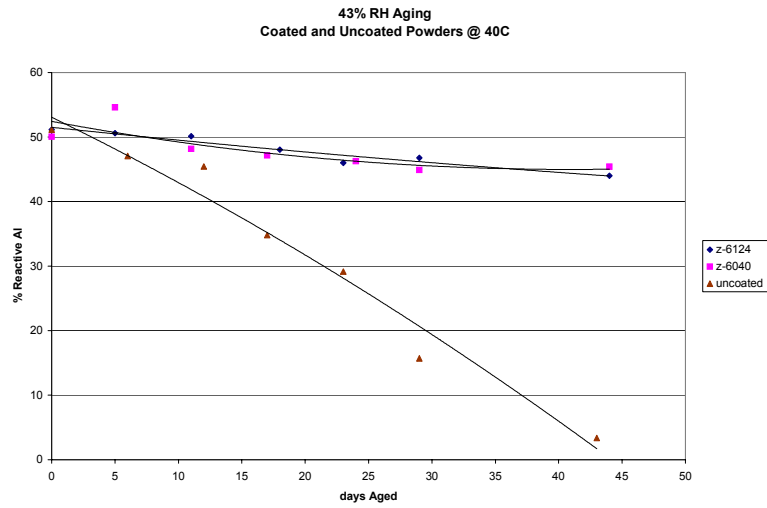


Figure 7. Aging results for coated and uncoated Al at 43 %RH.

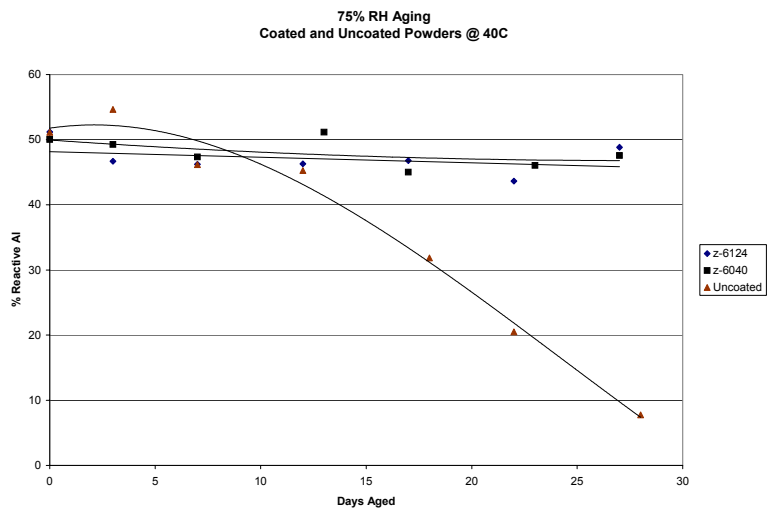


Figure 8. Aging results for coated and uncoated Al at 75 %RH.

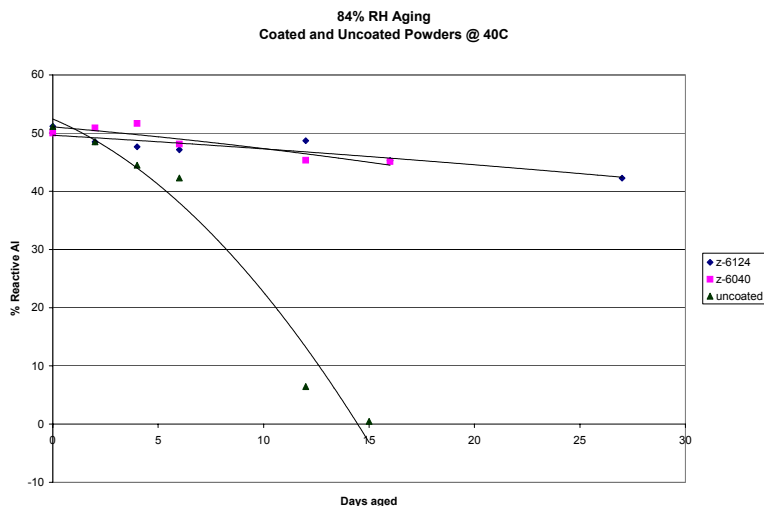


Figure 9. Aging results for coated and uncoated Al at 84 %RH.

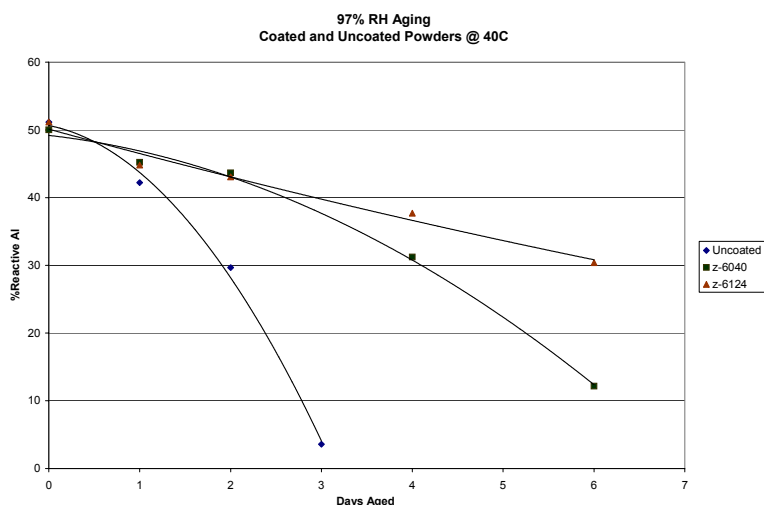


Figure 10. Aging results for coated and uncoated Al at 97 %RH.

Silane coating of aluminum nanopowders results in several-fold decrease of aging rate as compared to an untreated material. Both silanes are similarly effective at RH <85%. The Z6124 silane appeared as more effective coating than Z6040 silane only at very high relative humidity.

Work is underway to determine the amount of silane (or other coating agents) that has bonded (chemically or via adsorption) to the surface of the nanopowders. The experiments will make use of the coating agent solution concentration before and after the powders have been dispersed in the solution. To eliminate the coating agent that maybe adsorbed, the powders will then be washed in pure solvent and the solvent analyzed to determine if the coating agent is present. Currently Dow Corning Z-6124 Silane is being examined by UV-Vis. UV-Vis is being used for

it's ease and short analysis time. The unique structure of this silane allows for analysis in the UV range. Z-6124 is phenyltrimethoxysilane. The phenyl group shows relatively strong absorption in the 260-275 nm range.

Although the 43 % RH samples react slower than those at higher humidities, a nearly 60 percent decrease in the reactive aluminum content in 50 days is still significant. A relative humidity of 43 percent is not an unusual ambient reading. If not adequately sealed from the environment, a dramatic decrease in the reactivity of aluminum nano-powders or reactive systems utilizing aluminum will be experienced.

It was found that the curves in above presented figure initially show a flat slope with little decrease in the percent reactive aluminum. A steep slope corresponding to a dramatic decrease in the percent reactive aluminum follows the flat portion of the curve. In the flat region of the curve it is believed that hydration of the existing oxide layer is taking place. Once the existing layer has been hydrated, reaction of the core (unreacted aluminum) begins, which is represented by the sharp increase in the slope of the curves.

Similar results for hydration were shown by Grimblot and Eldridge [1], which they termed an incubation period (IP). In their research the oxidation of Al was monitored by weight change of aluminum samples immersed in aqueous solutions. Aluminum oxide layers were formed on the aluminum samples prior to immersion in solution. It was found that when placed in aqueous solution, aluminum samples with oxide layers formed in a dry environment show a period of no weight change, or an IP, followed by a fast rate of weight change. However, samples prepared with a hydrated oxide layer did not exhibit the IP but immediately began to show a fast rate of weight change. Grimblot and Eldridge believe that the hydrated Al_2O_3 structure is more open allowing for easier movement of diffusing species (i.e. water).

Similar results were found when aging samples of 50 nm Nanotechnologies and 51 nm Technanogy aluminum in 97 %RH at 40 °C. The results are shown in Figure 11 below. The Nanotechnologies sample shows a period of little to no change in percent reactive aluminum until around 26 hours, while the Technanogy sample shows immediate decreases in percent reactive aluminum after 8 hours. Samples of both powders were analyzed for water content using TGA. It was found that the Technanogy sample contained between 7 and 8 wt% water. The Nanotechnologies sample only contained around 3 wt% water. It is likely that the oxide layer of the Technanogy sample is more hydrated compared to the Nanotechnologies sample.

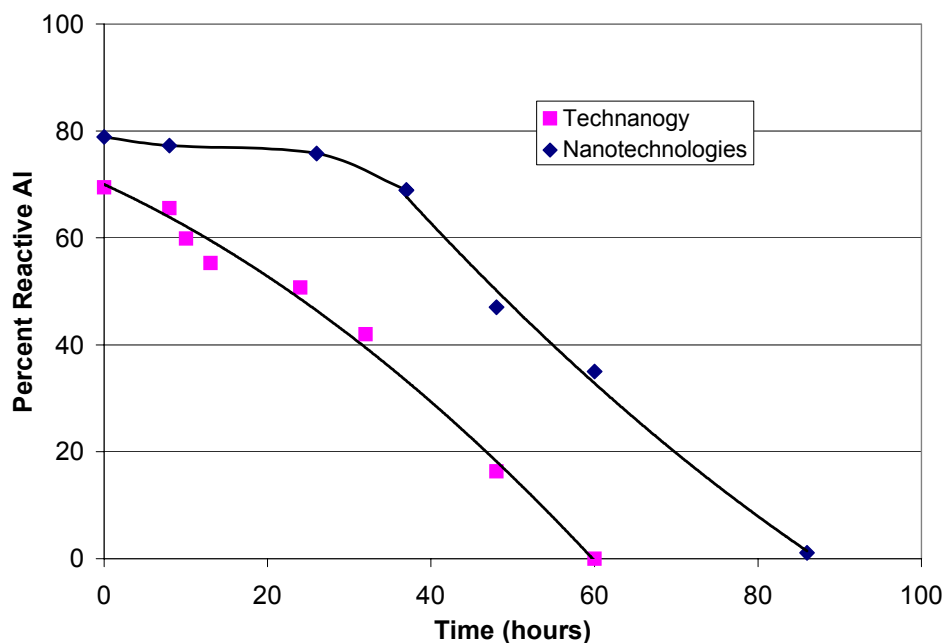


Figure 11: Results for aging of Nanotechnologies and Technanogy aluminum samples in 97 %RH at 40 °C. Lines shown are trendlines only and each data point is an average of two volumetric method measurements.

5. MIXING OF NANOSIZE ALUMINUM AND TITANIUM DIOXIDE POWDERS.

The objective of the experiment was twofold:

- To study the formation of agglomeration and the quality of mixing;
- to compare hexane and ethanol as solvent for nanosized powder systems.

Aluminum and titanium dioxide powders were chosen as the model reacting system. Assuming the same particle size of aluminum and titanium dioxide powders and considering the difference in the density of these two materials (Al 2.7 g/cm³ and TiO₂ 4.26 g/cm³) a mixture of such two powders in weight ratio equal to 1:1 molar ratio, will has the property to occupy the similar volume by each of the components. Volume calculation based on the stated assumptions result in a Aluminum: Titanium dioxide ratio of 41:59. This weight ration was kept constant for all experiments.

Preparation of the samples.

Absolute ethanol and n-hexane from stock was used as a solvent. Two weight % of Sodium dioctyl sulfosuccinate (“Aerosol OT 100% Surfactant” from Cytec Industries Inc.) was added as surfactant to each solution.

0.00269g of Al and 0.00599g of TiO₂ was added each solution. The dispersions were mixing in an ultrasonic bath for 20 minutes. After mixing, powder mixtures were dried on aluminum plate and sample were taken with an adhesive carbon tape. The carbon tapes were placed on specimen holders and carbon coated.

SEM/Microprobe analyses.

SEM and Microprobe analyses followed: First, secondary electron images (which have a good resolution) and backscattered electron images (which provide better contrast) were taken at 10000X. (Figures 12,13 and 14,15). However, those images do not take the surface roughness into account.

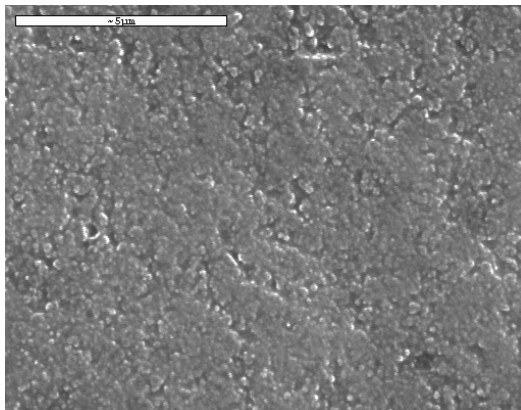


Figure 12. Al-TiO₂-mixture prepared in absolute ethanol with sodium dioctyl sulfosuccinate as surfactant (SE-image 10000 X).

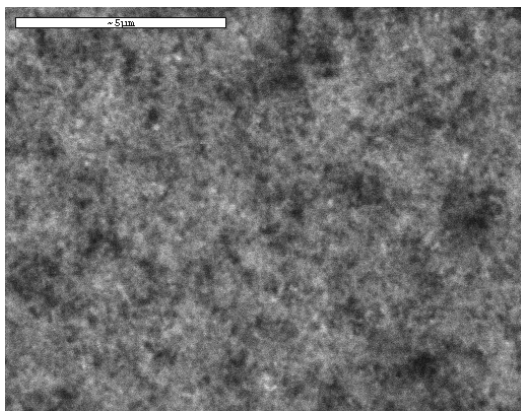


Figure 13. Al-TiO₂-mixture prepared in absolute ethanol with sodium dioctyl sulfosuccinate as surfactant (BSE-image 10000 X).

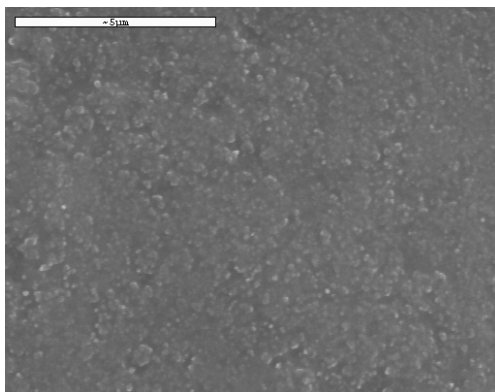


Figure 14. Al-TiO₂-mixture prepared in n-hexane with sodium dioctyl sulfosuccinate as surfactant (SE-image 10000 X).

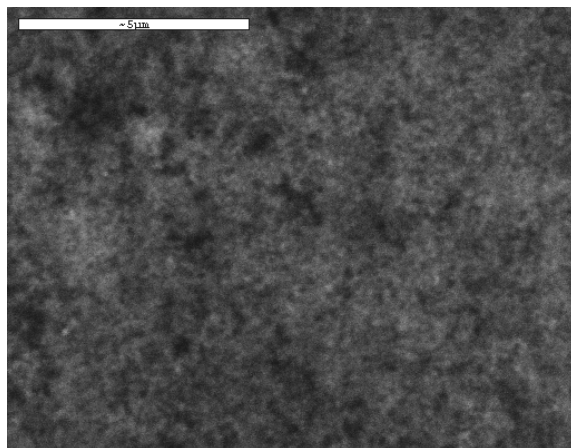


Figure 15. Al-TiO₂-mixture prepared in n-hexane with sodium dioctyl sulfosuccinate as surfactant (BSE-image 10000 X).

After that, so called cameo images were taken as first screening. The Cameo Image technique is a half-quantitative imaging technique developed by Oxford Inc., combining SE-image signal with energy dispersive x-ray analysis (see Figures 16 and 17). However just the overall energy values of a sample are taken into account and not the specific peak of element. In our case, the energy value of aluminum is lower than the energy peaks of titanium, so we can paint the dots, which have lower energy value (Al) red and dots, which exhibit higher energy value blue (Ti). The green color represents mixed areas.

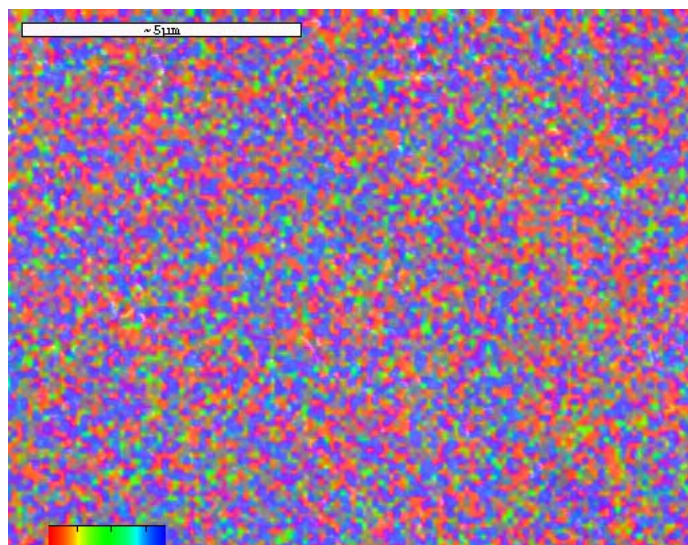


Figure 16: Al-TiO₂-mixture prepared in absolute ethanol with sodium dioctyl sulfosuccinate as surfactant (Cameo-image 10000 X).

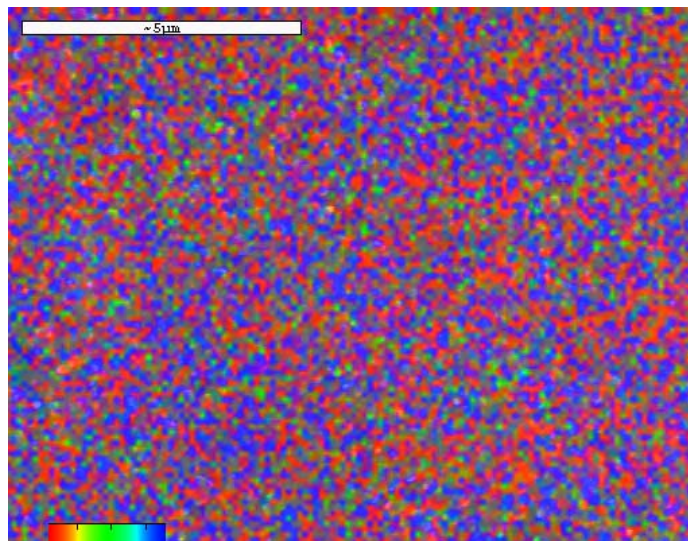


Figure 17. Al-TiO₂-mixture prepared in n-hexane with sodium dioctyl sulfosuccinate as surfactant (Cameo-image 10000 X).

The microprobe elemental analysis were conducted as mapping tests and as line scans, by using the strongest energy disperse peaks of aluminum and titanium.

The mapping was taken at a magnification of 10000X. Figures 18 and 19 show SE-images, BSE-images, elemental Al –images, and elemental Ti -images. This overview allows distinguishing between surface roughness (shadow effects) and agglomerations.

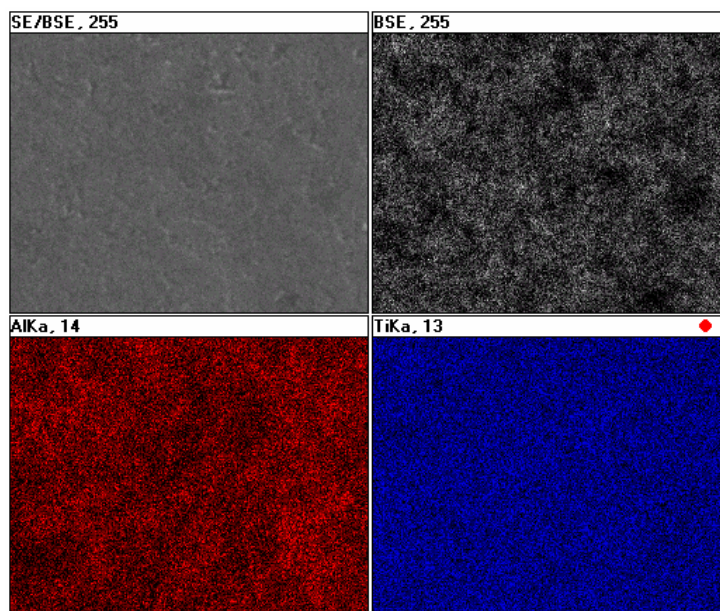


Figure 18. Al-TiO₂-mixture prepared in absolute ethanol with sodium dioctyl sulfosuccinate as surfactant (Elemental Mapping 10000 X SE-BSE-Al and Ti mapping image).

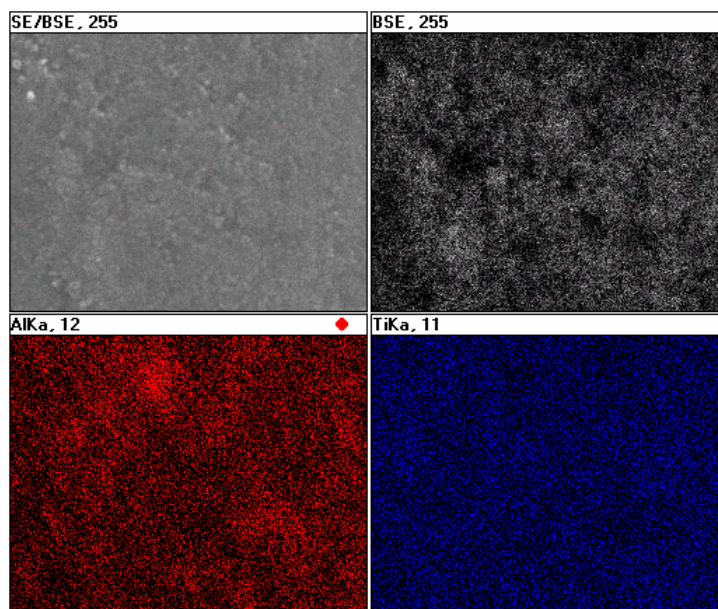


Figure 19. Al-TiO₂-mixture prepared in *n*-hexane with sodium dioctyl sulfosuccinate as surfactant (Elemental Mapping 10000 X SE-BSE-Al and Ti mapping image).

The line scan pick up the presence of both elements at the same time and allows for a quantitative comparison of the x-ray energy signals, which can be relates to the weight and atomic percentage of the elements present in the sample. Examples of the line-scan are shown in Figures 20 and 21.

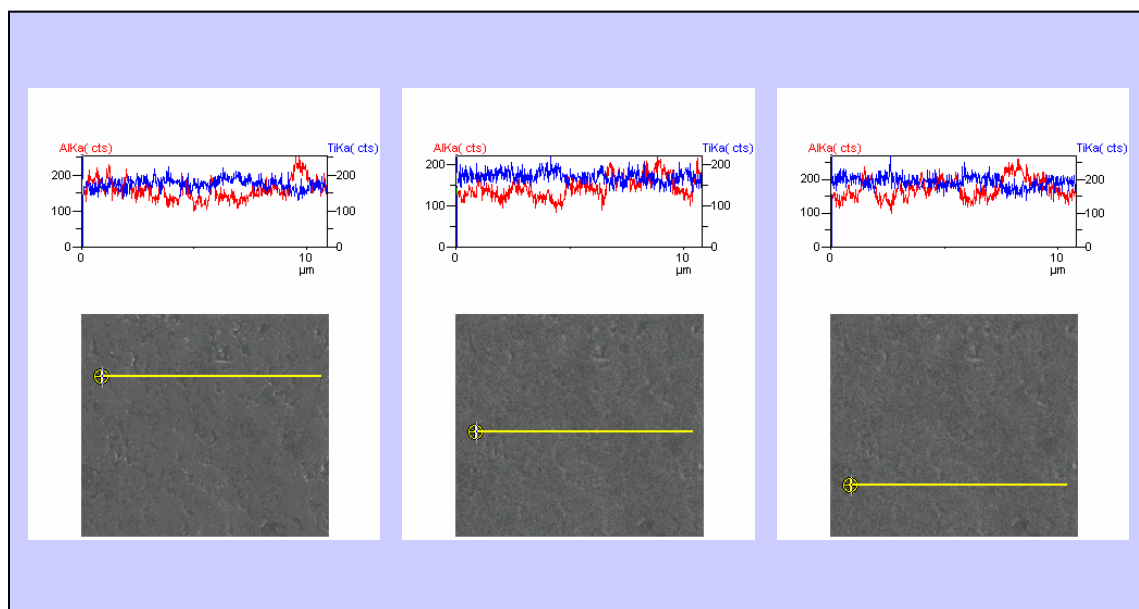


Figure 20. Al-TiO₂-mixture prepared in absolute ethanol with sodium dioctyl sulfosuccinate as surfactant (Three line scans of 10 μm at 10000 X).

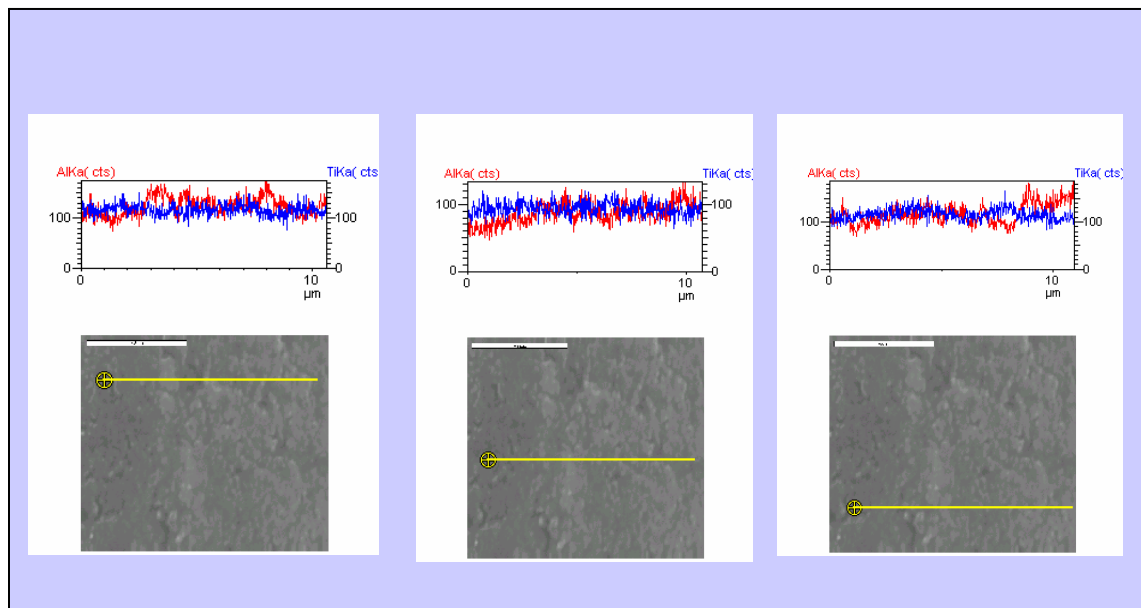


Figure 21. Al-TiO₂-mixture prepared in n-hexane with sodium dioctyl sulfosuccinate as surfactant (Three line scans of 10 μm at 10000 X).

It was interesting to notice that long in time line scans (100s) lead to reaction of the samples (see Figures 22 and 23), whereas the mapping or the cameo analyses (scanning a whole area) leaves the sample as it is. It should be further noted that that the sample prepared with abs. ethanol (Figure 23) shows a bigger effect than the sample prepared with n-hexane (Figure 24). Obviously the intensity (energy /area*time) of the electron beam was sufficient to promote a reaction. The subsequent spot analysis conducted at the sample which was prepared with ethanol, proves that there are differences in the composition of the areas where lines scan were made (Figure 23: spot #1 and #4) and where no lines scans were made (Figure 23: spot #2 and #3). However, how these changes finally affect the results was not further investigated due to safety reasons.

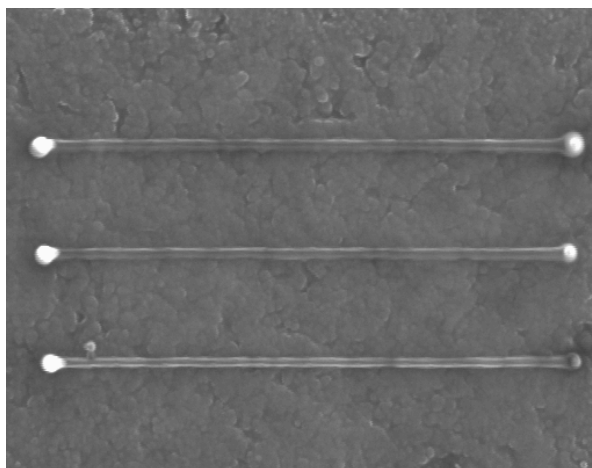


Figure 22. Al-TiO₂-mixture prepared in absolute ethanol with sodium dioctyl sulfosuccinate as surfactant. Sample after three line scans of 10 μm at 10000 X.

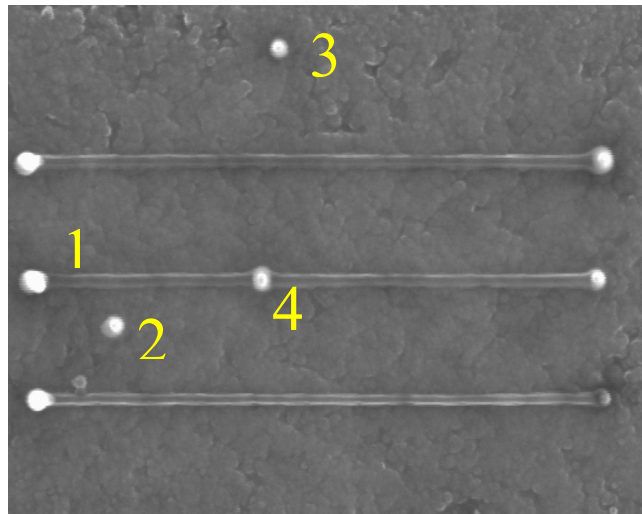


Figure 23. Al-TiO₂-mixture prepared in absolute ethanol with sodium dioctyl sulfosuccinate as surfactant. Sample after three line scans of 10 μm at 10000 X. The X-ray spot analyses at four points for aluminum and titanium show the following results #1 (Al: 44.7 Ti: 55.3), #2 (Al: 48.4 Ti: 51.6), #3 (Al: 48.8 Ti: 51.2), #4 (Al: 40.8 Ti: 59.2).

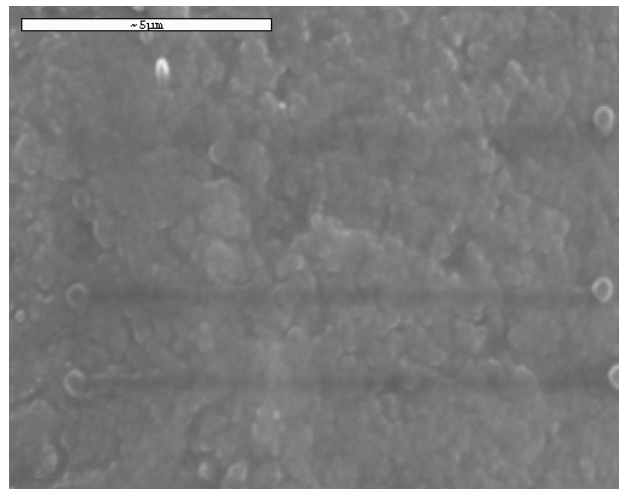


Figure 24. Al-TiO₂-mixture prepared in n-hexane with sodium dioctyl sulfosuccinate as surfactant. Sample after the three line-scans of 10 μm at 10000 X.

The mixing technique with ethanol seems to work better based on the qualitative results. However, the resulting mixture seems to be also more reactive. The next step of these mixing experiments will be the testing of combustion velocity of those powder mixtures.

5. MEASUREMENTS OF PROPAGATION VELOCITIES.

Combustion front propagation velocity for unconfined reactive powders is one of the indirect measures of the inhomogeneous reaction rate and the reactant affinity. Propagation

velocities in Al-CuO and Al-MoO₃ reacting systems were found to have, very high combustion front velocities. Moreover, due to a rapid expansion of gases generated at very high temperatures in Al-CuO and Al-MoO₃ systems, unreacted powders ahead of the combustion front are frequently expelled from the burn tray's cavity. Because of this displacement, the measured combustion velocities might be erratic. In order to countermeasure this effect series of perforated baffles was inserted into the trough to minimize powder displacement. The propagation velocities in the Al-CuO system, measured without the use of baffles, varied from 100 m/s to 1000 m/s. However, when baffles were used, the combustion front velocities in the same system were consistent and significantly lower (250 ± 25 m/s). Table 3 shows the average combustion front velocities in Al-CuO reacting systems in an air atmosphere.

Table 3. Average propagation velocity of the investigated systems under unconfined conditions.

Reacting System (Nanosize Powders)	Atmosphere	Combustion Front Velocities [m/s]
Al 50 nm(Nanotechnologies Inc) and CuO (Nanophase Tech)	Air	416 ± 25
Al 80 nm(Nanotechnologies Inc) and CuO (Nanophase Tech)	Air	500 ± 25

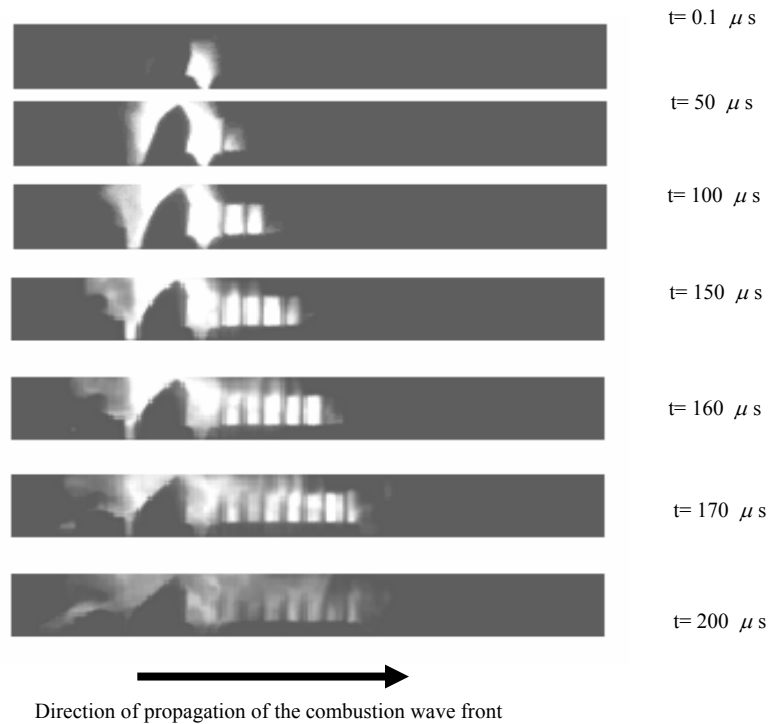


Figure 25. Images of burning loose nanopowders of Al-MoO₃ system recorded, with perforated baffles, using high-speed camera.

Figure 25 shows typical images of a combustion front propagation in the Al-MoO₃ system. The recording rate was 8,000 fps with a shutter speed of 1/128,000 s. Bright plumes, shown in the images, are likely composed of metal vapor and alumina particulates when the combustion was carried out in an inert atmosphere. When the thermite reaction took place in air, a significant plume was formed due to the secondary reaction between generated vapor and gaseous oxygen.

Silane and oleic acid coatings prove to be effective at preventing the aging of aluminum nano-powders but it was not known what affect they would have on the reactivity of MIC reactant mixtures (specifically aluminum/copper oxide) containing coated aluminum. Samples of aluminum containing 0, 1, 3, 5, 10, and 15 wt% silane were mixed with CuO and tested for propagation velocity in open burn tray measurements. The results can be seen in Table 4 and Figure 26 below.

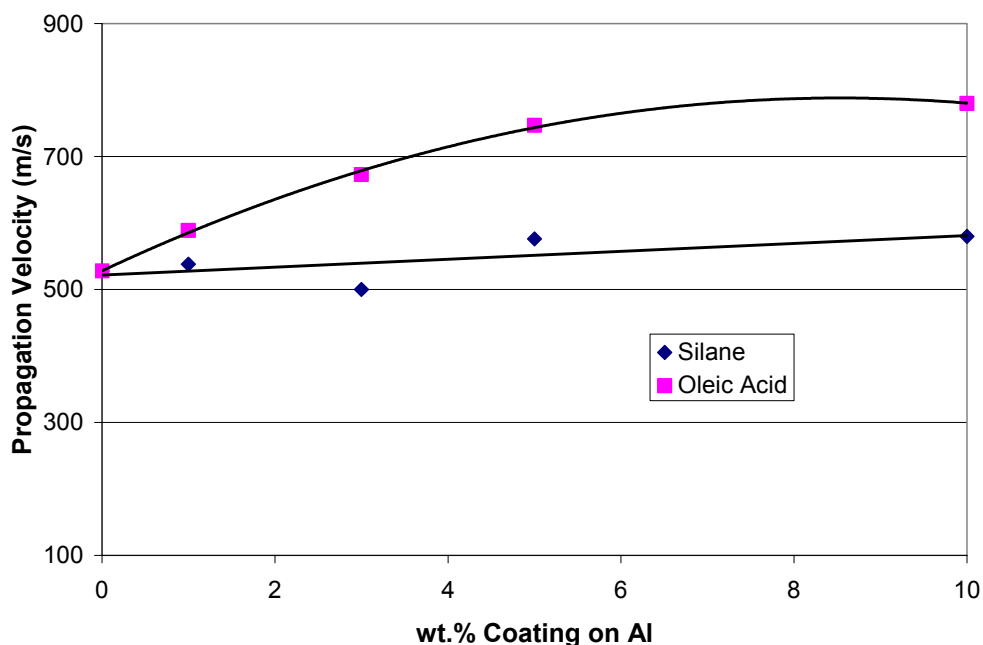


Figure 26. Results for the measurement of propagation velocity of Al/CuO as a function of weight percent coating on the aluminum nano-powder. The coatings used were Z6124 silane and oleic acid. Each data point is the average of 4 measurements.

Table 4. Results for the measurement of propagation velocity of Al/CuO as a function of weight percent coating on the aluminum nano-powder. The coatings used were Z6124 silane and oleic acid.

	Z6124 Silane		oleic acid	
Weight % Coating	*Propagation Velocity (m/s)	Std dev (m/s)	*Propagation Velocity (m/s)	Std dev (m/s)
0	528	27	528	27
1	538	30	589	49
3	500	46	673	67
5	576	47	747	56
10	580	70	780	14
15	no ignition	-----	no ignition	-----

*Each data point is an average of 4 measurements.

It is shown as oleic acid concentration is increased up to 10 weight percent there is a dramatic increase in the propagation velocity. In all, there is almost a 50 % increase in propagation velocity for the 10 weight percent sample compared to the uncoated sample. Data appears to be leveling off between 5 and 10 weight percent and at 15 weight percent oleic acid ignition does not take place. This indicated there is an optimal concentration around 10 weight percent.

The Z6124 silane coated samples show a similar but less dramatic trend. In fact if the standard deviation is taken into account the velocities measured cannot be considered different with any reasonable confidence. As was seen with oleic acid, the 15 weight percent sample also was unable to ignite.

Propagation velocity is increased due to enhanced mixing of the reactants with increased coating concentration. It is now known for 50 nm aluminum that Z6124 silane in excess of 3 wt% is not chemically bonded to the aluminum and would disperse in the mixing solvent (hexane). The excess silane then acts as a surfactant improving mixing between both reactants. The bonded silane acts as a surfactant as well, helping to suspend the aluminum particles in solution. However, as the coating concentration increases the coating layer begins to thicken. The coating creates an additional barrier between reactants that must be removed for reactants to come into contact. This increase in the barrier works in opposition to the enhancement of mixing, and at 15 wt% coatings are in too large a concentration and prevent contact between the aluminum and copper oxide reactants. If the reactants are not in contact ignition is not possible.

Furthermore the oleic acid shows improvement over Z6124 silane for three reasons. First physisorption is more likely to take place for oleic acid than chemisorption. The physisorb oleic acid molecules disperse in the mixing solvent and can contact both the aluminum and copper oxide particles equally. The second reason is the long 18-member oleic acid tail has greater molecular interaction with the straight chain hexane molecule than the phenyl group on the Z6124 Silane. The enhanced interaction makes oleic acid a better surfactant improving mixing

of the reactants. The final reason is that after hydrolysis of the silane to form silanol, self-condensation of silanol can occur to form siloxane linkages. The formation of the siloxane linkages may create an additional barrier (in the form of a siloxane layer) that needs to be broken down for reaction to occur.

To help support the above hypothesis of improved mixing, a second set of experiments were performed using oleic acid and 1-6341 silane, designated n-octyltriethoxysilane. 1-6341 has a straight 8-member hydrocarbon chain as its organic group. It was assumed that 1-6341 would have improved mixing capability over Z6124 because of the long carbon chain, which should have stronger interaction with hexane. In this experiment the aluminum powders were not coated prior to mixing. The “coating” was added, at various concentrations, directly to hexane during the mixing of the Al/CuO reactants. The amounts of coating added were exactly the same as the amounts present in the previous experiments. The mixed powders were dried and the coating remained on the powders. The results were as expected, as coating concentration increase propagation velocity increased for both oleic acid and 1-6341 silane. Comparing these results to the previous experiments, the percent increase in propagation velocity from lowest concentration to highest concentration (10 wt%) is still close to 50 % for oleic acid. Also as expected, 1-6341 silane was an improvement over Z6124 silane. Comparing the results of the 0 and 10 wt% concentrations, 1-6341 silane had a 40 % increase in propagation velocity compared to less than a 10 % increase for Z6124 silane. The results are shown in Figure 27 below.

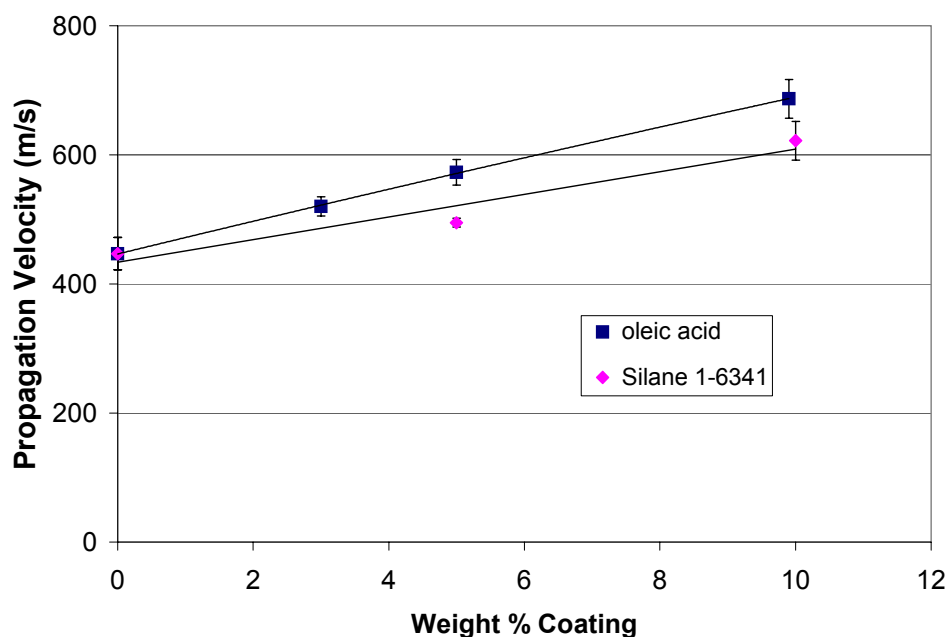


Figure 27. Propagation velocity as a function of coating concentration.
Coatings were added at the time of mixing of Al/CuO reactants.

Effect of Coating on Ignition delay

It was initially expected that coatings on aluminum nano-powder would add an additional barrier that needed to be removed for reactants to contact and reaction to progress. Experiments were performed in which the weight percent coating on aluminum was varied and the ignition

delay time of Al/CuO, mixed using these coated powders, was measured. Both oleic acid and Z6124 silane were tested.

It is observed that the silane coating affects the ignition delay to a greater degree than oleic acid. The ignition delay was 2.5 times greater for the 7 wt% coating of silane on aluminum than the uncoated aluminum sample. In comparison, ignition delay of the 10 wt% oleic acid coated aluminum was only 1.4 times greater than uncoated aluminum. The results are shown in Figure 28 below. The overall results were as expected however; coatings on aluminum nanopowder increase the ignition delay of Al/CuO. The coatings add an additional barrier that must be removed for reaction to initiate. Just as the aluminum oxide layer must be removed for reactants to come into contact, the coating must be removed. Additional energy is required to remove the coating layer.

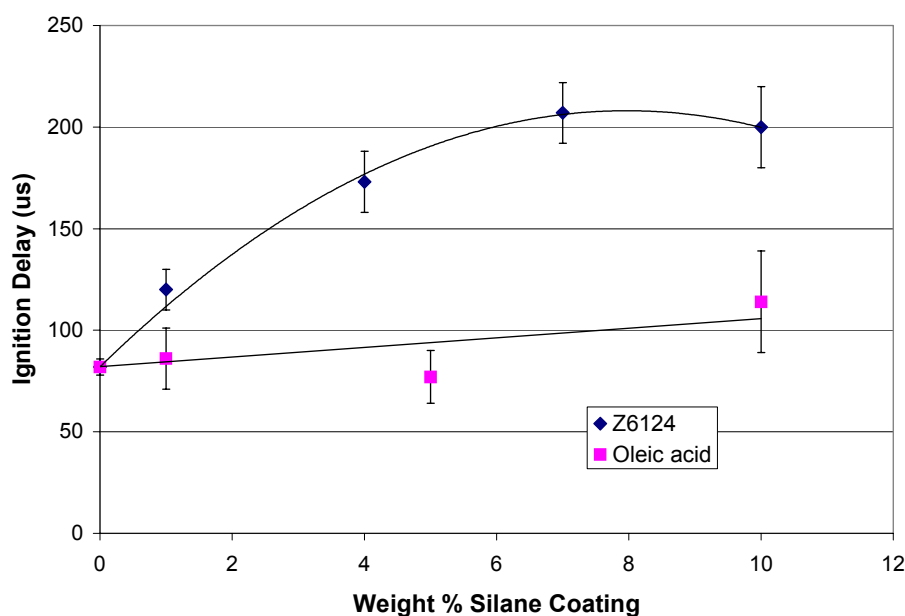


Figure 28. Al/CuO ignition delay results for coated aluminum sample. Coatings studied were Z6124 Silane and oleic acid.

5. MATHEMATICAL MODELING OF CONDENSED-PHASE COMBUSTION.

Two different models for analyses of combustion-wave propagation in condensed phase reactions were examined in these research studies:

- I. Condensed-phase reactions without significant vaporization of reactants and products;
- II. Condensed-phase reactions with significant vaporization of reactants and products.

The objective was to investigate on 1-D model for both condensed phase reactions with and without significant vaporization.

Mathematical model for condensed-phase reaction without significant vaporization of reactants and products

In the first model, the mathematical model was done in a cylindrical reacting sample along which the self-propagating high temperature combustion wave occurs. Figure 29 shows the cylindrical sample over which the material and energy balance were modeled [2].

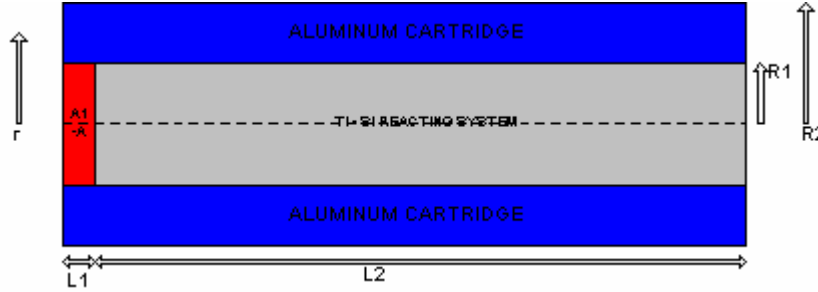


Figure 29. Schematic of the cylindrical reacting sample.

The material balance over the cylindrical reacting sample mixture is given by:

$$\frac{\partial \eta_p}{\partial t} = \phi(\eta, T) \quad (1)$$

The energy balance over the reacting sample mixture is:

$$\rho_s C p_s \frac{\partial T}{\partial t} = \frac{\partial \left(k_s \frac{\partial T}{\partial z} \right)}{\partial z} + \frac{\rho_s W_{frac}}{M} (-\Delta H_{Rp}) (\phi(\eta, T)) \quad (2)$$

Dimensional analysis for condensed-phase reaction without significant vaporization of reactants and products

Due to computational advantages it was decided that Equations 1 and 2 should be rewritten into a dimensionless form. The heat release function $\phi(\eta, T)$ is typically represented as:

$$\phi(\eta, T) = f(\eta_p) f(T) \quad (3)$$

where:

$$f(\eta) = 1 - \eta_p \quad (4)$$

$$f(T) = k_o \exp\left(-\frac{E}{RT}\right) \quad (5)$$

Eq.5 could be approximated using Frank-Kamenetskii approximation [3] written as:

$$\exp\left(-\frac{E}{RT}\right) = \exp\left(-\frac{E}{RT_c}\right) \exp\left(\frac{E(T-T_c)}{RT_c^2}\right) \quad (6)$$

in which T_c represent the combustion or ignition temperature. It was decided that the dimensionless temperature had to be driven from Eq.6 and could be defined as:

$$\Theta = \frac{T-T_c}{T_c} \quad (7)$$

Substituting Eq.7 into Eq.6 gives:

$$\exp\left(-\frac{E}{RT}\right) = \exp\left(-\frac{E}{RT_c}\right) \exp\left(\frac{E}{RT_c} \Theta\right) \quad (8)$$

It was decided that

$$\Re = \exp\left(\frac{E}{RT_c}\right) \quad (9)$$

Thus, Eq.8 become:

$$\exp\left(-\frac{E}{RT}\right) = \Re^{(\Theta-1)} \quad (10)$$

Solving for T from Eq.7 gives:

$$T = T_c(\Theta + 1) \quad (11)$$

Furthermore, the dimensionless length was defined as:

$$\xi = \frac{z}{L} \quad (12)$$

Thus, the differential operators for Eq.11 and 12 are:

$$dT = T_c d\Theta \quad dz = L d\xi \quad (13, 14)$$

Rewriting Eq.2 in term of dimensionless temperature and length result into:

$$\rho_s C_p T_c \frac{\partial \Theta}{\partial t} = \frac{k_s T_c}{L^2} \frac{\partial^2 \Theta}{\partial \xi^2} + \frac{\rho_s W_{frac} k_o}{M} (-\Delta H_{Rp}) f(\eta_p) (\Re^{(\Theta-1)}) \quad (15)$$

Simplifying Eq.15 gives:

$$\frac{\partial \Theta}{\partial t} = \frac{k_s}{\rho_s C p_s L^2} \frac{\partial^2 \Theta}{\partial \xi^2} + \frac{W_{frac} \rho_s k_o}{\rho_s C p_s M T_c} (-\Delta H_{Rp}) f(\eta_p) \Re^{(\Theta-1)} \quad (16)$$

The dimensionless time and its differential operator were defined as:

$$\tau = \frac{t}{t^*} \quad dt = t^* d\tau \quad (17, 18)$$

where:

$$t^* = \frac{\rho_s C p_s L^2}{k_s} \quad (19)$$

Eq.16 could be rewritten as:

$$\frac{\partial \Theta}{\partial \tau} = \frac{\partial^2 \Theta}{\partial \xi^2} + \Psi f(\eta_p) \Re^{(\Theta-1)} \quad (20)$$

where:

$$\Psi = \frac{W_{frac} L^2 \rho_s k_o (-\Delta H_{Rp})}{k_s M T_c} \quad (21)$$

The dimensionless form for mass balance is:

$$\frac{\partial \eta_p}{\partial \tau} = t^* k_o f(\eta_p) \Re^{(\Theta-1)} \quad (22)$$

Boundary and initial conditions

Initial conditions are:

$$\tau = 0 \quad 0 < \xi < 1: \quad \Theta = \frac{T_o - T_c}{T_c}, \quad \eta = 0$$

The boundary conditions can be represented as follows:

$$\begin{aligned} \tau > 0 \quad \xi = 0: \quad \Theta &= 0 \\ \xi = 1: \quad \frac{d\Theta}{d\xi} &= 0 \end{aligned}$$

Crank-Nicolson Implicit Scheme Method

It was decided to use a numerical discrete Crank-Nicolson implicit scheme for approximation of time and spatial derivatives in both energy and mass balances equations [4-8]:

$$\frac{\eta_{p,i}^{n+1} - \eta_{p,i}^n}{\Delta \tau} = t^* k_o f(\eta_{p,i}^n) \Re^{(\Theta_i^n - 1)} \quad (23)$$

Furthermore, Eq.20 after discrization becomes:

$$\frac{\Theta_i^{n+1} - \Theta_i^n}{\Delta \tau} = \left[\frac{\Theta_{i+1}^{n+1} - 2\Theta_i^{n+1} + \Theta_{i-1}^{n+1}}{2(\Delta \xi)^2} + \frac{\Theta_{i+1}^n - 2\Theta_i^n + \Theta_{i-1}^n}{2(\Delta \xi)^2} \right] + \Psi_i^n f(\eta_{p,i}^n) \Re^{(\Theta_i^n - 1)} \quad (24)$$

Matrix-free Approximation

In order to develop a code for the generalized equations, it was decided that a matrix form for Eq.24 is necessary to solve the above system of equations. It was further decided that the conversion (Eq.23) has to be calculated at later time steps to avoid complication of Eq.24. Thus, Eq.23 was written explicitly. Simplifying Eq.24 gives:

$$A_i^n \Theta_{i-1}^{n+1} + B_i^n \Theta_i^{n+1} + C_i^n \Theta_{i+1}^{n+1} = D_i^n \quad (25)$$

Where:

$$A_i^n = -\frac{\Delta \tau}{2\Delta \xi^2} \quad (26)$$

$$B_i^n = 1 + \frac{\Delta \tau}{\Delta \xi^2} \quad (27)$$

$$C_i^n = -\frac{\Delta \tau}{2\Delta \xi^2} \quad (28)$$

$$D_i^n = \Theta_i^n + \Delta \tau \left[\frac{\Theta_{i+1}^n - 2\Theta_i^n + \Theta_{i-1}^n}{2\Delta \xi^2} \right] + \Delta \tau \Psi_i^n (1 - \eta_{p,i}^n) \Re^{(\Theta_i^n - 1)} \quad (29)$$

Applying grids for $i = 1, 2, \dots, m$ to Eq.25 result into a matrix (see Fig.30).

$$\begin{bmatrix} B_1 & C_1 & & & & & \\ A_2 & B_2 & C_2 & & & & \\ & A_3 & B_3 & C_3 & & & \\ & & \bullet & \bullet & \bullet & & \\ & & & \bullet & \bullet & \bullet & \\ & & & & \bullet & \bullet & \bullet \\ & & & & & A_{m-1} & B_{m-1} & C_{m-1} \\ & & & & & & A_m & B_m \end{bmatrix} \begin{bmatrix} \Theta_1 \\ \Theta_2 \\ \Theta_3 \\ \Theta_4 \\ \bullet \\ \Theta_{m-2} \\ \Theta_{m-1} \\ \Theta_m \end{bmatrix} = \begin{bmatrix} D_1 \\ D_2 \\ D_3 \\ \bullet \\ \bullet \\ \bullet \\ D_{m-1} \\ D_m \end{bmatrix}$$

Figure 30. Tridiagonal matrixes for energy equation (Eq.25).

This is a tridiagonal system i.e. a system of equations with finite coefficient only on the main diagonal (the B_i 's), the lower diagonal (the A_i 's), and the upper diagonal (the C_i 's).

A standard method for solving a system of linear, algebraic equations is Gaussian elimination. Thomas' algorithm is essentially the result of applying Gaussian elimination to the tridiagonal system of equations. A code was written in FORTRAN language to solve Eq.23 and the above matrix. The developed code was then incorporated into a window format using Visual basic (See Fig.31). The code for the above equations was named **1-D implicit (open system)** as seen on Fig.31. However, more testing is necessary on the window version to make it user friendly.

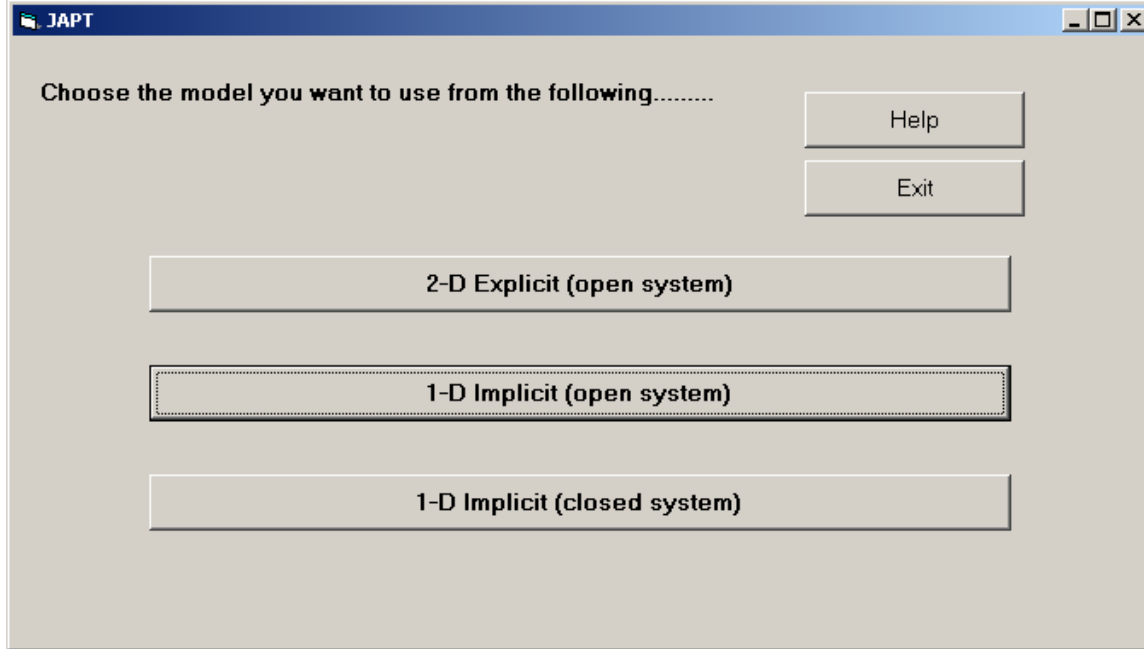


Figure 31. Screen shoot of window version.

Numerical Results

Initially, the model was tested for non-reacting cylindrical sample. The frequency factor, length of non-reacting cylindrical sample, integral time, ignition, and initial temperatures were set to 0s^{-1} , 0.0254m , 0.004 , 2000K , and 300K respectively. Figure 32 shows the temperature profile along the length of the non-reacting sample for various times. It can be seen that in non-reacting cylindrical sample, the sample was only being heated.

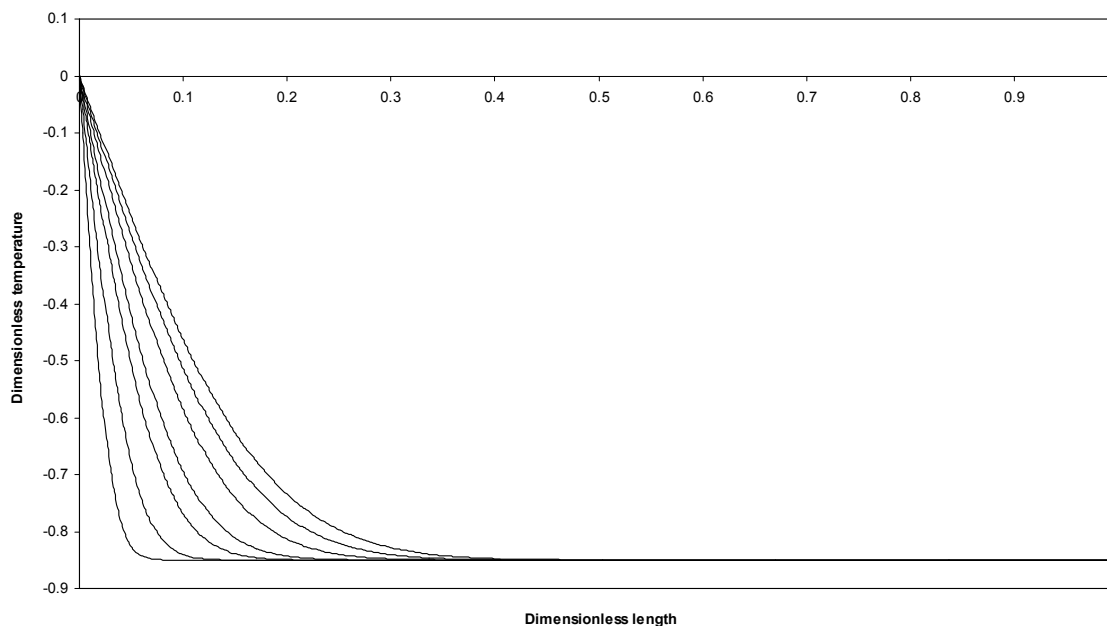


Figure 32. Temperature profile in a non-reacting cylindrical sample with $\Delta\tau = 0.004$.

Secondly, a reacting cylindrical sample was considered in which the frequency factor was set to $1.44\text{E}10\text{s}^{-1}$ with the rest of the parameters being the same as in non-reacting sample. The code generates the temperature and conversion profile along the cylindrical sample (see Figure 33).

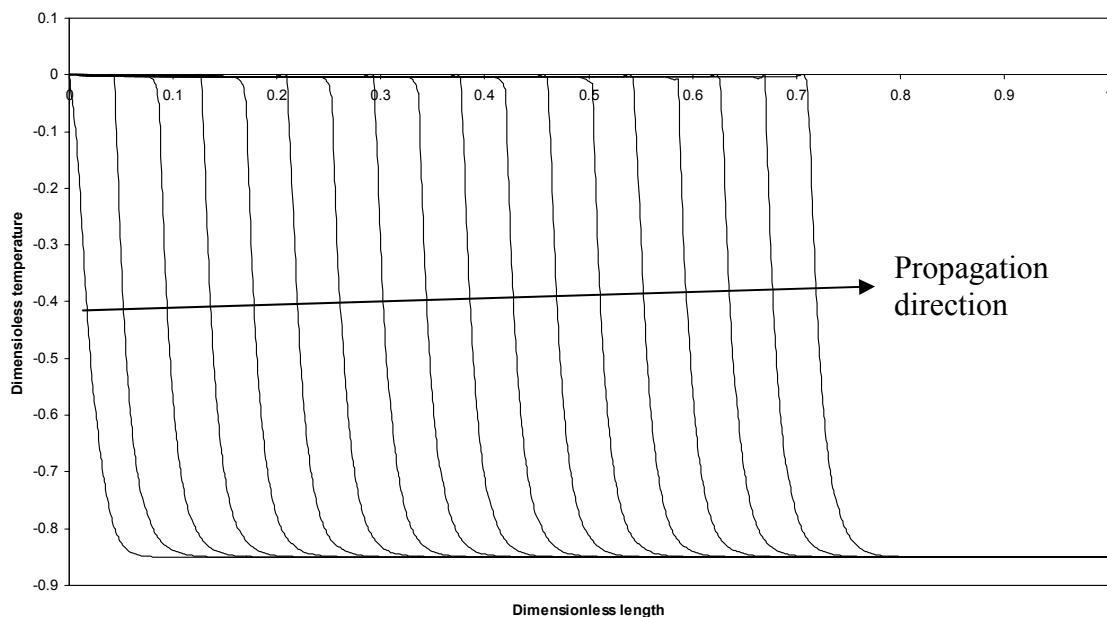


Figure 33. Temperature profile in the cylindrical sample with $\Delta\tau = 0.004$.

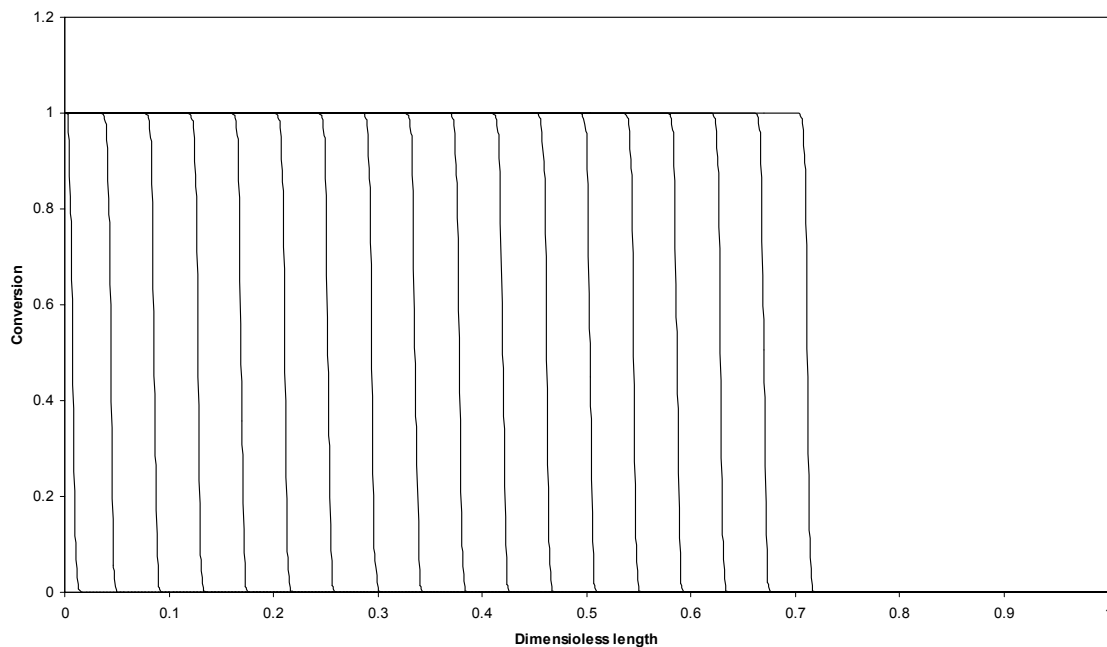


Figure 34. Conversion profile in the cylindrical sample with $\Delta\tau = 0.004$.

To further the investigation, the length of the cylindrical sample was kept at 0.0254 m and the pre-exponential factor was increased to $1.728\text{E}10\text{s}^{-1}$ and $2.016\text{E}10\text{s}^{-1}$ respectively. These changes were made to investigate the effect of pre-exponential factor along the length of cylindrical sample. The dimensionless temperature profiles that show these changes are shown in Figures 35 and 36.

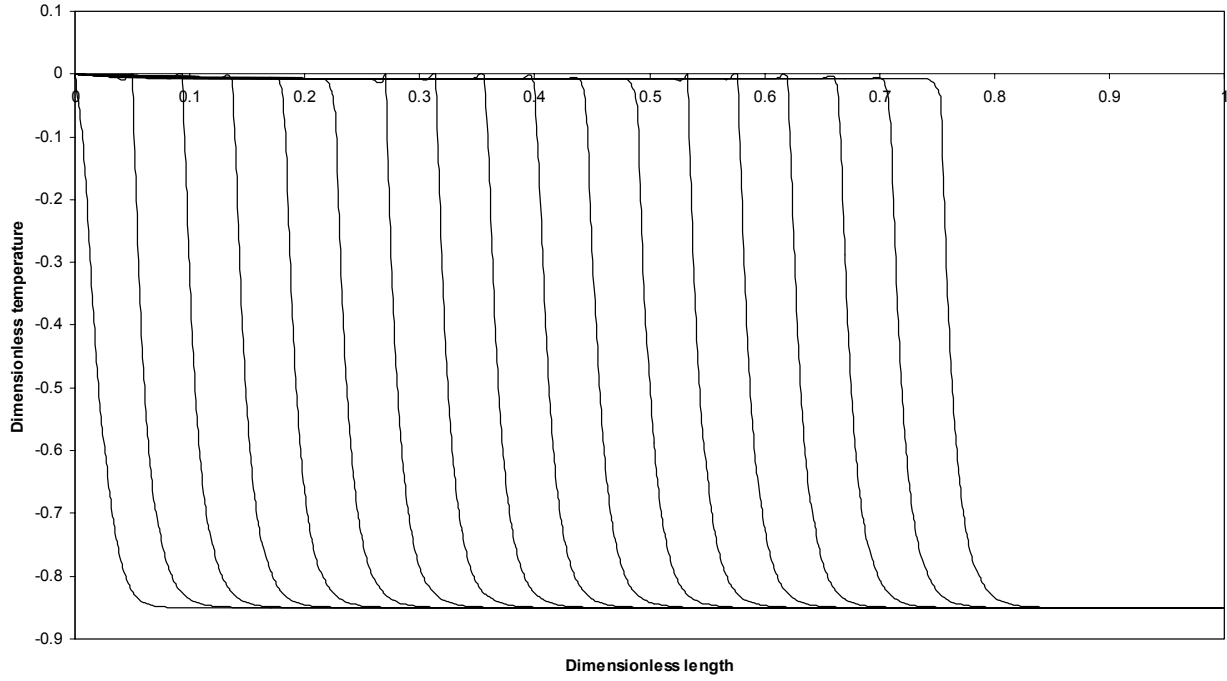


Figure 35. Temperature profile in a reacting cylindrical sample for frequency factor of $1.728E10s^{-1}$ with $\Delta\tau = 0.002$.

It can be seen from Figures 35 and 36 that as the pre-exponential factor is increased the propagation become faster. Figure 37 shows the temperature profile for pre-exponential factor of $2.016e10s^{-1}$.

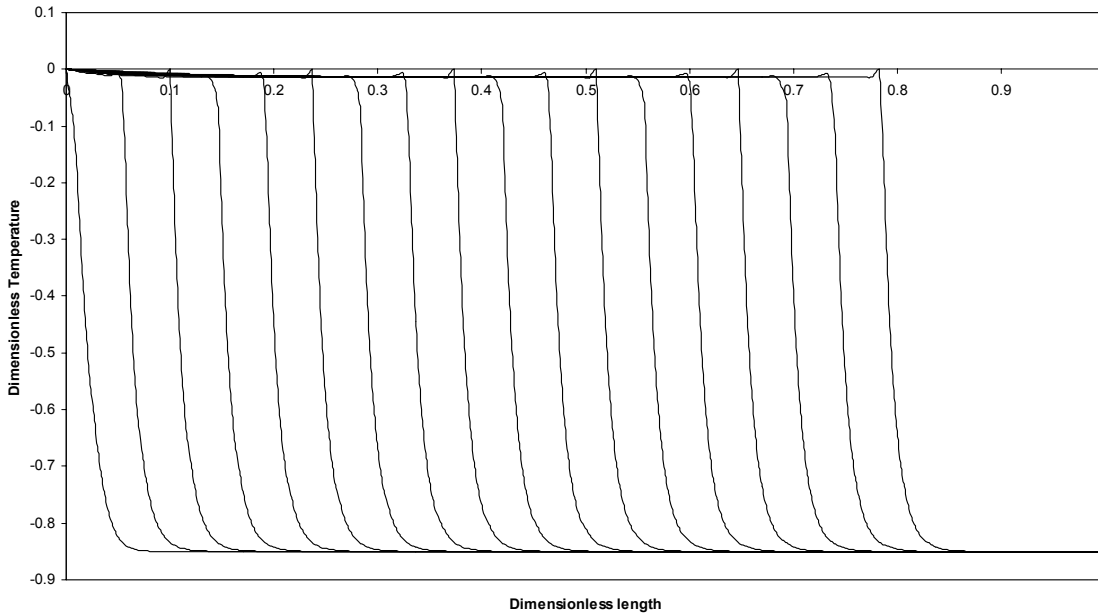


Figure 37. Temperature profile in the reacting cylindrical sample for frequency factor of $2.016e10s^{-1}$ with $\Delta\tau = 0.002$.

Mathematical model of combustion front propagation under the presence of uniaxial gas pressure gradient

In many cases temperatures generated during the combustion are very high causing partial or complete vaporization of product(s). A mathematical model describing propagation characteristics in a condensed-phase system with significant pressure generation behind a combustion front was developed and explored.

A one dimensional adiabatic model is presented below. The subscript *s* denotes the solid phase and the subscript *g* denotes the gas phase.

$$\overline{\rho C_p} \frac{\partial T}{\partial t} + v_g \rho_g C_{p_g} \frac{\partial T}{\partial z} = \frac{\partial}{\partial z} \left(k_s \frac{\partial T}{\partial z} \right) + \frac{\rho_s W_{frac}}{M} (-\Delta H_{Rp}) \phi(\eta_p, T) \quad (30)$$

where:

$$\overline{\rho C_p} = (1 - \Phi) \rho_s C_{p_s} + \Phi \rho_g C_{p_g} \quad (31)$$

$$C_{p_g} = \alpha + \beta T + \gamma T^2 \quad (32)$$

The material balance over cylindrical sample is given by:

$$\frac{\partial \eta_p}{\partial t} = \phi(\eta_p, T) \quad (34)$$

Where $\phi(\eta_p, T)$ was given by Eq.3 rewritten as:

$$\phi(\eta, T) = f(\eta_p) f(T) \quad (3)$$

The continuity equation over the cylindrical sample was defined as [9]:

$$\frac{\partial \rho_g}{\partial t} + \frac{(\rho_g v_g)}{\partial z} = 0 \quad (35)$$

It was decided that the pressure drop along the cylindrical sample could be evaluated using Ergun equation given by [10]:

$$\frac{dP}{dz} = - \frac{G}{\rho_g g_c D_p} \left(\frac{(1 - \Phi)}{\Phi^3} \right) \left[\frac{150(1 - \Phi)\mu}{D_p} + 1.75G \right] \quad (36)$$

where:

$$G = \rho_g \Phi v_g \quad (37)$$

Substituting Eq.37 into Eq.36 gives:

$$\frac{dP}{dz} = -\frac{v_g}{g_c D_p} \left(\frac{(1-\Phi)}{\Phi^2} \right) \left[\frac{150(1-\Phi)\mu}{D_p} + 1.75\rho_g \Phi v_g \right] \quad (38)$$

In Eq.38 the only parameter that changes with pressure is the density of the gas. It was further decided that the mass flow rate at any point down the reactor is constant. Furthermore, it was decided that the gas used in this system is an inert. Thus, the density of the gas was defined as:

$$\rho_g = \rho_{g_o} \left(\frac{T_o}{T} \right) \left(\frac{P}{P_o} \right) \quad (39)$$

Substituting Eq.39 for density into Eq.38 gives:

$$\frac{dP}{dz} = -\frac{v_g}{g_c D_p} \left(\frac{(1-\Phi)}{\Phi^2} \right) \left[\frac{150(1-\Phi)\mu}{D_p} + 1.75\rho_{g_o} \left(\frac{T_o}{T} \right) \left(\frac{P}{P_o} \right) \Phi v_g \right] \quad (40)$$

In addition to Eq.39 that relates the density, pressure, and temperature, it was further decided that the gas used in the system behave ideally. Further relation between density, pressure, and temperature was given by ideal gas law written as:

$$\rho_g = \frac{P}{RT} \quad (41)$$

In addition to the above equations, it was decided that the porosity could be formulated as

$$\Phi = \Phi_o + \Delta\Phi \eta_p \quad (42)$$

Where Φ_o and $\Delta\Phi$ are the initial and change of porosity respectively.

Dimensional analysis of the condensed-phase reaction with significant vaporization of reactants and products

Defining the dimensionless variables, the heat released function given by Eq.3 had been previously defined in a dimensionless form:

$$\phi(\eta_p, T) = k_o f(\eta_p) \Re^{(\Theta-1)} \quad (43)$$

Thus, the temperature, length, and their differential operators are given by

$$T = T_c (\Theta + 1) \quad \xi = \frac{z}{L} \quad dT = T_c d\Theta \quad dz = L d\xi \quad (44)$$

Rewriting the energy equation, Eq.30, into dimensionless length and temperature results:

$$\overline{\rho C_p T_c} \frac{\partial \Theta}{\partial t} + \frac{v_g \rho_g C_p T_c}{L} \frac{\partial \Theta}{\partial \xi} = \frac{T_c}{L^2} \frac{\partial}{\partial \xi} \left(k_s \frac{\partial \Theta}{\partial \xi} \right) + \frac{\rho_s W_{frac}}{M} (-\Delta H_{Rp}) (\phi(\eta_p, T)) \quad (45)$$

Simplifying Eq.45 gives:

$$\frac{\partial \Theta}{\partial t} + \frac{v_g \rho_g C_{p_g}}{L \overline{\rho C p}} \frac{\partial \Theta}{\partial \xi} = \frac{k_s}{L^2 \overline{\rho C p}} \frac{\partial^2 \Theta}{\partial \xi^2} + \frac{\rho_s W_{frac}}{M_i \overline{\rho C p} T_c} (-\Delta H_{Rp}) (\varphi(\eta, T)) \quad (46)$$

where:

$$\overline{\rho C p} = (1 - \Phi_o) \rho_s C_{p_s} + \Phi_o \rho_{g_o} C_{p_g} \quad (47)$$

The dimensionless velocity, density and time were defined as:

$$t^* = \frac{\overline{\rho C p} L^2}{k} \quad \tau = \frac{t}{t^*} \quad v^* = \frac{v_g}{v_o} \quad \rho^* = \frac{\rho_g}{\rho_{g_o}} \quad dt = t^* d\tau \quad (48)$$

Thus, Eq.46 could be rewritten in dimensionless form as:

$$\frac{\partial \Theta}{\partial \tau} + \Lambda \frac{\partial \Theta}{\partial \xi} = \frac{\partial^2 \Theta}{\partial \xi^2} + Y f(\eta) \Re^{(\Theta-1)} \quad (49)$$

where:

$$Y = \frac{L^2 \rho_s W_{frac} (-\Delta H_{Rp}) k_o}{M_i k_s T_c} \quad (50)$$

$$\Lambda = \frac{v_o \rho_{g_o} L v^* \rho^* C_{p_g}}{k_s} \quad (51)$$

Where v_o is the speed of sound and it was defined as:

$$v_o = \sqrt{\gamma R T_o} \quad (52)$$

The material balance in dimensionless form was defined as:

$$\frac{\partial \eta_p}{\partial \tau} = t^* k_o f(\eta_p) \Re^{(\Theta-1)} \quad (53)$$

The dimensionless form of continuity equation was written as:

$$\frac{\partial \rho^*}{\partial \tau} + \Omega \frac{\partial (\rho^* v^*)}{\partial \xi} = 0 \quad (54)$$

where:

$$\Omega = \frac{v_o t^*}{L} \quad (55)$$

The dimensionless pressure is defined as:

$$p^* = \frac{p}{p_o} \quad (56)$$

Thus, the dimensionless form of Ergun equation, Eq.40 was defined as:

$$\frac{dp^*}{d\xi} = -\frac{150(1-\Phi)^2 v_o L \mu}{p_o g_c D_p^2 \Phi^2} v^* - \frac{1.75 v_o^2 L}{g_c R D_p T_c} \left(\frac{(1-\Phi)}{\Phi} \right) \left(\frac{p^*}{\Theta+1} \right) v^{*2} \quad (57)$$

Eq.57 was simplified into a quadratic form written as:

$$\alpha v^{*2} + \beta v^* + \frac{dp^*}{d\xi} = 0 \quad (58)$$

where:

$$\alpha = \frac{1.75 v_o^2 L}{g_c R D_p T_c} \left(\frac{(1-\Phi)}{\Phi} \right) \left(\frac{p^*}{\Theta+1} \right) \quad (59)$$

$$\beta = -\frac{150(1-\Phi)^2 v_o L \mu}{p_o g_c D_p^2 \Phi^2} \quad (60)$$

The ideal gas law in dimensionless form was defined as:

$$\rho^* = \zeta \frac{p^*}{\Theta+1} \quad (61)$$

where:

$$\zeta = \frac{T_o}{T_c} \quad (62)$$

Boundary and initial conditions

The initial conditions are:

$$\tau = 0 \quad 0 < \xi < 1: \quad \Theta = \frac{T_o - T_c}{T_c}, \quad p^* = 1, \quad \eta = 0, \quad v^* = 0$$

The boundary conditions are:

$$\tau > 0 \quad \xi = 0: \quad \Theta = 0, \quad p^* = \frac{p_h}{p_o}$$

$$\xi = 1: \quad \frac{d\Theta}{d\xi} = 0, \quad \frac{dp^*}{d\xi} = 0$$

Discrete Crank-Nicolson Implicit Scheme Method

In this section the discrete Crank-Nicolson implicit solutions for Eq.49 through Eq.61 were formulated. This results in a nonlinear system of algebraic equations. A clear understanding of these nonlinear algebraic systems of equations is essential for describing the unique way in which we solve them.

Using a simple first order in time (backward Euler), second order in space discretization on a uniform grid, a discrete version of energy equation (Eq.49) was written as:

$$\left(-\frac{\Delta\tau\Lambda_i^n}{2\Delta\xi}-\frac{\Delta\tau}{2(\Delta\xi)^2}\right)\Theta_{i-1}^{n+1}+\left(1+\frac{\Delta\tau\Lambda_i^n}{2\Delta\xi}+\frac{\Delta\tau}{(\Delta\xi)^2}\right)\Theta_i^{n+1}+\left(-\frac{\Delta\tau}{2(\Delta\xi)^2}\right)\Theta_{i+1}^{n+1}=\Gamma_i^n \quad (63)$$

where:

$$\Gamma_i^n = \Theta_i^n - \Delta\tau\Lambda_i^n \left[\frac{\Theta_i^n - \Theta_{i-1}^n}{2\Delta\xi} \right] + \Delta\tau \left[\frac{\Theta_{i+1}^n - 2\Theta_i^n + \Theta_{i-1}^n}{2(\Delta\xi)^2} \right] + \Delta\tau Y_i^n f(\eta_{p_i}^n) \Re^{(\Theta_i^n-1)} \quad (64)$$

The material balance (Eq.53) after discretization gives:

$$\frac{\eta_{p_i}^{n+1} - \eta_{p_i}^n}{\Delta\tau} = t^* k_o f(\eta_{p_i}^n) \Re^{(\Theta_i^n-1)} \quad (65)$$

Discretization of continuity equation (Eq.54) gives:

$$\left(1 + \frac{\Delta\tau\Omega v_i^{*n}}{2\Delta\xi}\right)\rho_{*i}^{*n+1} - \frac{\Delta\tau\Omega v_i^{*n}}{2\Delta\xi}\rho_{*i-1}^{*n+1} + \frac{\Delta\tau\Omega\rho_i^{*n}}{2\Delta\xi}v_{*i}^{*n+1} - \frac{\Delta\tau\Omega\rho_i^{*n}}{2\Delta\xi}v_{*i-1}^{*n+1} = F_i^n \quad (66)$$

where:

$$F_i^n = \rho_{*i}^{*n} - \Delta\tau\Omega v_i^{*n} \left[\frac{\rho_{*i}^{*n} - \rho_{*i-1}^{*n}}{2\Delta\xi} \right] - \Delta\tau\Omega\rho_i^{*n} \left[\frac{v_{*i}^{*n} - v_{*i-1}^{*n}}{2\Delta\xi} \right] \quad (67)$$

The discrete Ergun equation (Eq.58) was written as:

$$\alpha_i^n (v_{*i}^{*n+1})^2 + \beta_i^n v_{*i}^{*n+1} + \frac{p_{*i}^{*n+1} - p_{*i-1}^{*n+1}}{2\Delta\xi} + \frac{p_{*i}^{*n} - p_{*i-1}^{*n}}{2\Delta\xi} = 0 \quad (68)$$

Discretization of ideal gas gives:

$$\rho_{*i}^{*n+1} = \zeta \frac{p_{*i}^{*n+1}}{\Theta_i^{n+1} + 1} \quad (69)$$

The porosity equation (Eq.5.11) was written as:

$$\phi_i^{n+1} = \phi_o + \Delta\phi\eta_i^n \quad (70)$$

Matrix-free Approximation

In this study the generalized Crank-Nicolson implicit scheme solutions were formulated into matrices. This formulation is useful in solving Equations 63 through 70. After simplifying Eq.63 gives:

$$X_i^n \Theta_{i-1}^{n+1} + \Sigma_i^n \Theta_i^{n+1} + K_i^n \Theta_{i+1}^{n+1} = \Gamma_i^n \quad (71)$$

where:

$$X_i^n = -\frac{\Delta \tau \Lambda_i^n}{2\Delta \xi} - \frac{\Delta \tau}{2(\Delta \xi)^2} \quad (72)$$

$$K_i^n = -\frac{\Delta \tau}{2(\Delta \xi)^2} \quad (73)$$

$$\Sigma_i^n = 1 + \frac{\Delta \tau \Lambda_i^n}{2\Delta \xi} + \frac{\Delta \tau}{(\Delta \xi)^2} \quad (74)$$

Applying the boundary conditions to Eq.71 result in a matrix (see Fig.38).

$$\begin{bmatrix} \Sigma_1 & K_1 & & & & & \\ X_2 & \Sigma_2 & K_2 & & & & \\ & X_3 & \Sigma_3 & K_3 & & & \\ & & \bullet & \bullet & \bullet & & \\ & & & \bullet & \bullet & \bullet & \\ & & & & \bullet & \bullet & \bullet \\ & & & & & X_{m-1} & \Sigma_{m-1} & K_{m-1} \\ & & & & & & X_m & \Sigma_m \end{bmatrix} \begin{bmatrix} \Theta_1 \\ \Theta_2 \\ \Theta_3 \\ \Theta_4 \\ \bullet \\ \bullet \\ \Theta_{m-2} \\ \Theta_{m-1} \\ \Theta_m \end{bmatrix} = \begin{bmatrix} \Gamma_1 \\ \Gamma_2 \\ \Gamma_3 \\ \bullet \\ \bullet \\ \bullet \\ \Gamma_{m-1} \\ \Gamma_m \end{bmatrix}$$

Figure 38. Resulted matrix for energy equation.

This is a tridiagonal system i.e. a system of equations with finite coefficient only on the main diagonal (the Σ_i 's), the lower diagonal (the X_i 's), and the upper diagonal (the K_i 's).

It was decided that the velocity of the gas at each grid point and time $\tau + \Delta \tau$ has to be evaluated using Eq.68.

$$v_{i,i}^{*n+1} = \frac{-\beta_i^n \pm \sqrt{\beta_i^{n^2} - 4\alpha_i^n \mathfrak{I}}}{2\alpha_i^n} \quad (75)$$

where:

$$\mathfrak{I} = \frac{p_{i,i}^{*n+1} - p_{i-1,i}^{*n+1}}{2\Delta \xi} + \frac{p_{i,i}^{*n} - p_{i-1,i}^{*n}}{2\Delta \xi} \quad (76)$$

As a result of this mathematical solution to velocity of the gas, the continuity equation can now be used to solve the density of the gas. After simplifying Eq.66 it becomes:

$$\lambda_i^n \rho_{i,i}^{*n+1} + \mathfrak{N}_i^n \rho_{i-1,i}^{*n+1} = H_i^n \quad (77)$$

where:

$$H_i^n = F_i^n - \Pi_i^n v_i^{*n+1} - \omega_i^n v_{i-1}^{*n+1} \quad (78)$$

$$\lambda_i^n = 1 + \frac{\Delta \tau \Omega v_i^{*n}}{2\Delta \xi} \quad \varsigma_i^n = -\frac{\Delta \tau \Omega v_i^{*n}}{2\Delta \xi} \quad (79)$$

$$\Pi_i^n = \frac{\Delta \tau \Omega \rho_i^{*n}}{2\Delta \xi} \quad \omega_i^n = -\frac{\Delta \tau \Omega \rho_i^{*n}}{2\Delta \xi} \quad (80)$$

Applying the boundary conditions for $i = 1, 2, \dots, m$ to Eq.77 result in the matrix shown in Figure 39.

$$\begin{bmatrix} \lambda_1 & & & & & & & \\ \varsigma_2 & \lambda_2 & & & & & & \\ & \varsigma_3 & \lambda_3 & & & & & \\ & & \bullet & \bullet & & & & \\ & & & \bullet & \bullet & & & \\ & & & & \bullet & \bullet & & \\ & & & & & \bullet & \bullet & \\ & & & & & & \varsigma_{m-1} & \lambda_{m-1} \\ & & & & & & & \varsigma_m \end{bmatrix} \begin{Bmatrix} \rho_1^* \\ \rho_2^* \\ \rho_3^* \\ \rho_4^* \\ \bullet \\ \bullet \\ \bullet \\ \rho_{m-2}^* \\ \rho_{m-1}^* \end{Bmatrix} = \begin{Bmatrix} H_1 \\ H_2 \\ H_3 \\ \bullet \\ \bullet \\ \bullet \\ H_{m-1} \\ H_m \end{Bmatrix}$$

Figure 39. Continuity equation matrix.

The pressure drop along the cylindrical sample was solved using the ideal gas law given by Eq.69. A code was written using FORTRAN program to perform the above calculations. The developed code was incorporated into window version and was named **1-D implicit (closed system)**.

Numerical results

Initially, the code was tested for non-reactive system. In this testing, the chamber was pressurized at 70 bars. A length of 0.0254 m of the cylindrical sample was used. The porosity, initial pressure, particle diameter, viscosity of the gas, density of the particle, activation energy, heat of reaction per mass of limiting reactant, thermal conductivity, and mass fraction of the limiting reactant were set to 0.4, 1.0 bar, 1.0e-5m, 2.29e-5 Pa.s, 2551.5 kg/m³, 227000 J/mol, 5.85e6 J/kmol, 0.59 W/m.K, and 0.60 respectively. The ignition and initial temperature were set to 2000K and 300K respectively. The change in porosity from Eq.70 was assumed to be 0.5. In addition to the mentioned parameters, the heat capacity of the gas during the testing was assumed to be constant and set to 520.43 J/kg.K. The code generates pressure, density, and temperature profiles with $\tau = 3.2$ for 100 iterations (see Figures 40, 41, and 42).

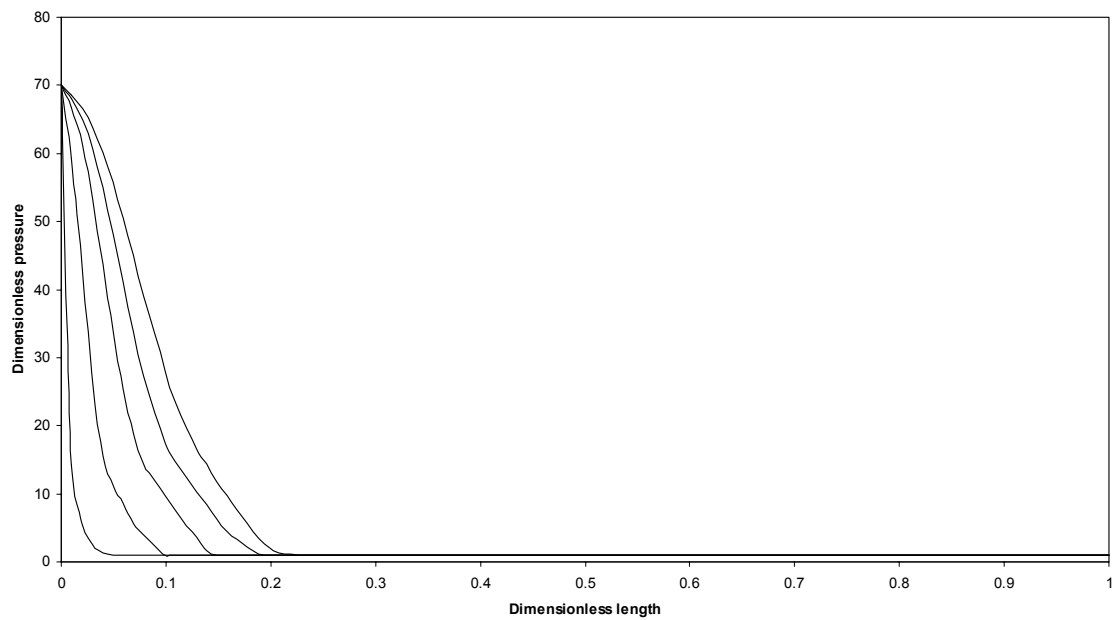


Figure 40. Dimensionless pressure profile for non-reacting system with $\Delta\tau = 0.005$.

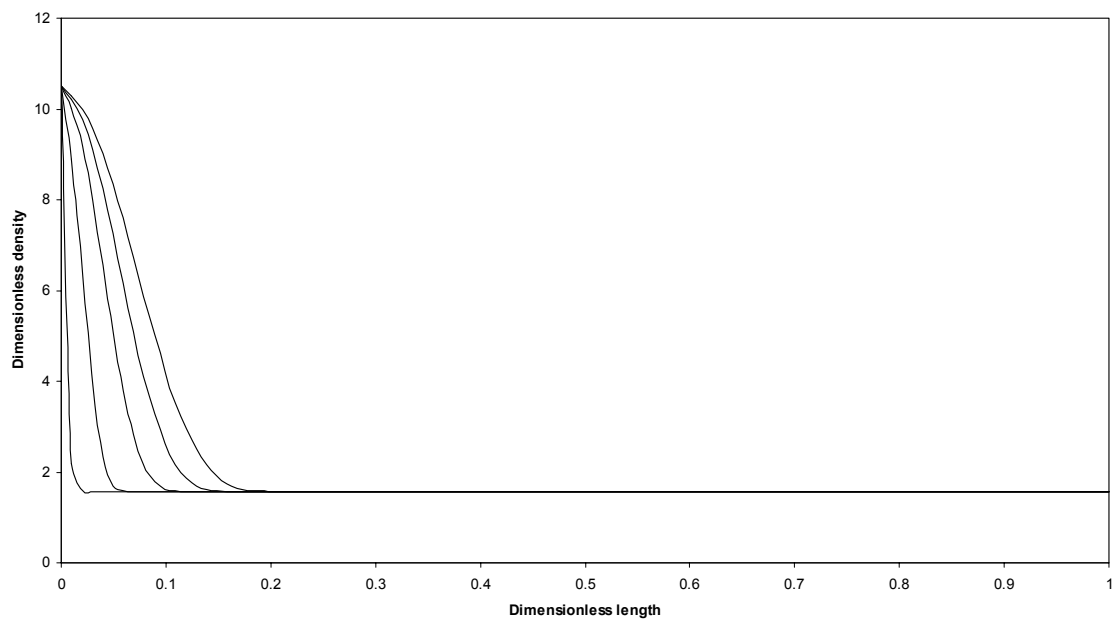


Figure 41. Dimensionless density profile for non-reacting system with $\Delta\tau = 0.005$.

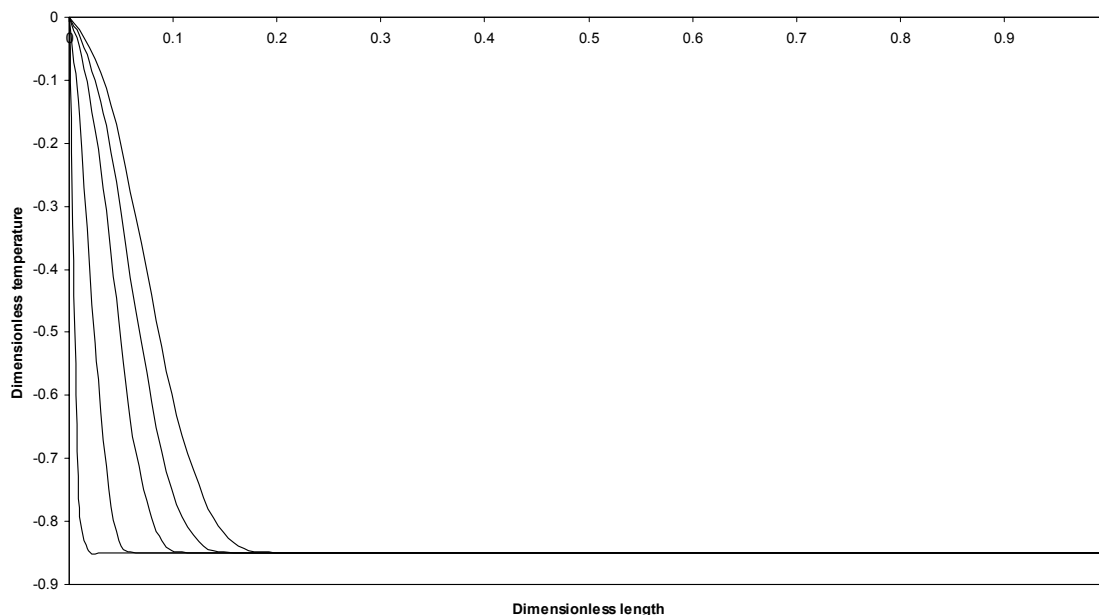


Figure 42. Dimensionless temperature profile for non-reacting system with $\Delta\tau = 0.005$.

Secondly, a reacting sample was considered in which the pre-exponential factor was set to $1.44 \times 10^{10} \text{s}^{-1}$. The pressure in the chamber was reduced to 50 bars and a sample length of 0.0254 m was considered. The sample was ignited at temperature of 2000 K. The calculated pressure, velocity, density, temperature, and the fraction of reactants reacted are shown in Figures 43-47.

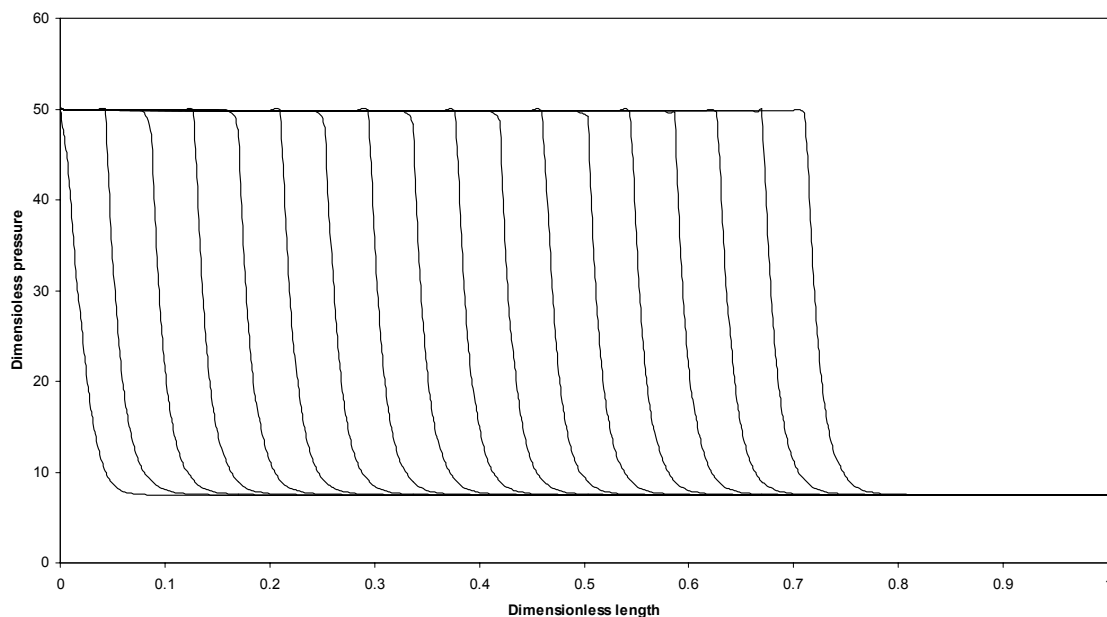


Figure 43. Dimensionless pressure profile with $\Delta\tau = 0.005$.

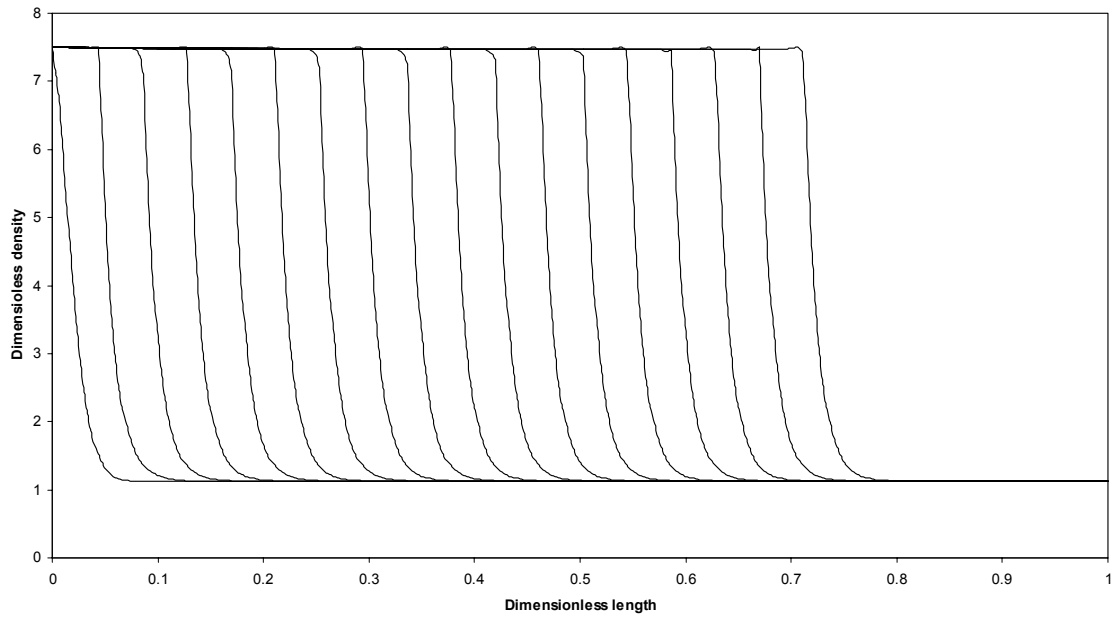


Figure 44. Dimensionless density profile for 50 bars (725 psi) with $\Delta\tau = 0.005$.

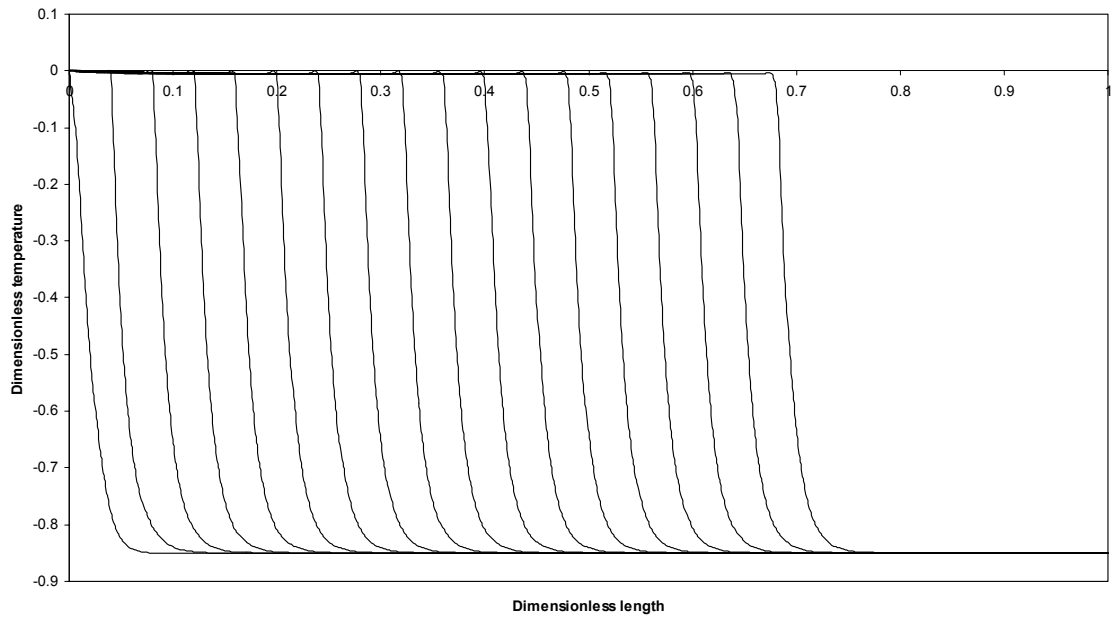


Figure 45. Dimensionless temperature profile for 50 bar (725 psi) with $\Delta\tau = 0.005$.

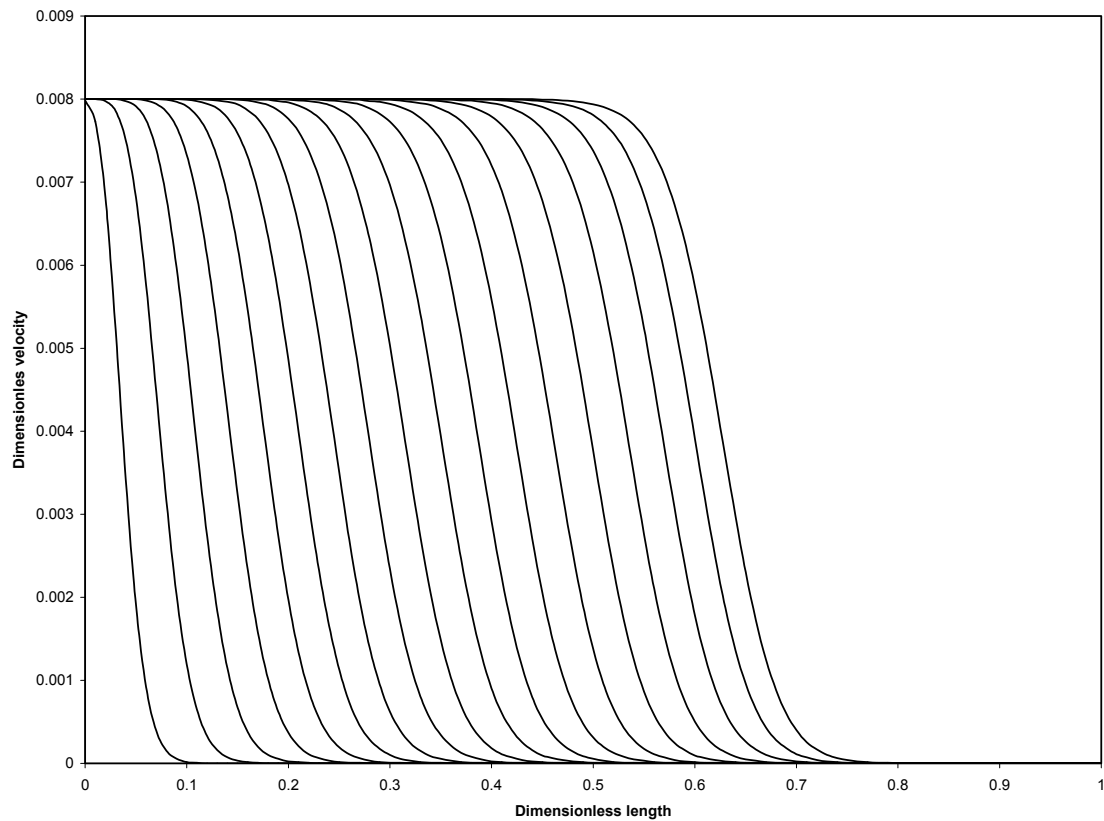


Figure 46. Dimensionless velocity profile for 50 bar (725 psi) with $\Delta\tau = 0.005$.

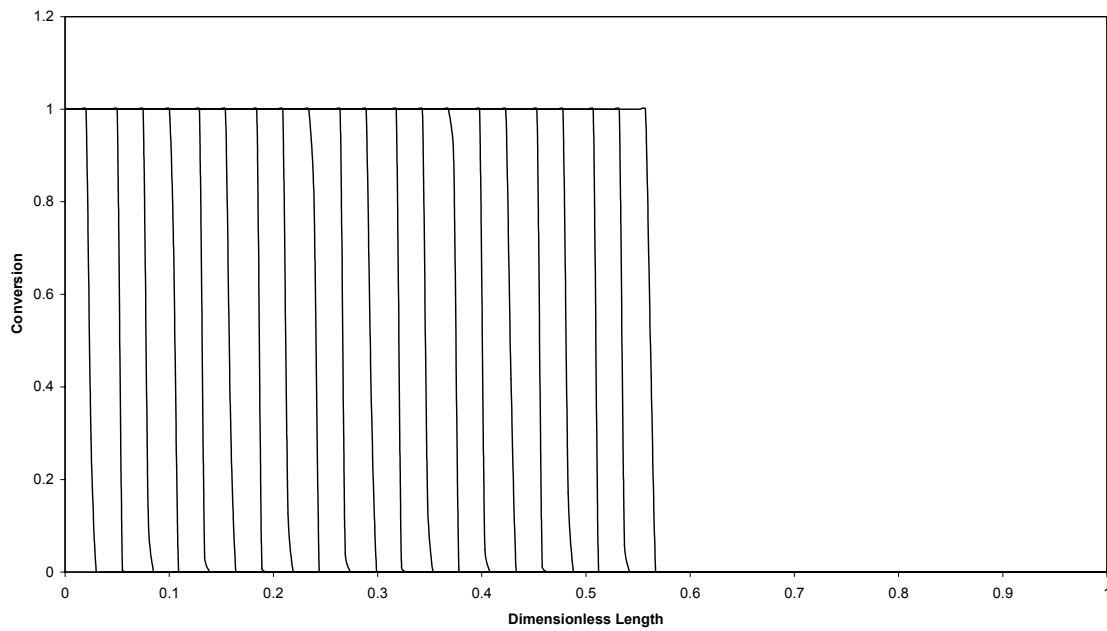


Figure 47. Conversion profile for 50 bar (725 psi) with $\Delta\tau = 0.005$.

In order to get a clear understanding of this system, a change in pressure was considered. The sample length was kept at 0.0254 m. The pressure inside the chamber was changed from 70 bar (1000 psi) to 140 bar (2000 psi). The rest of parameters were kept at the same conditions. The code generated the pressure, temperature, density, velocity, and conversion dynamic profiles. The results are shown on Figure 48-57, respectively. The velocity ratio was plotted at various pressures (725 -3000 psi) and the results are shown Figure 58.

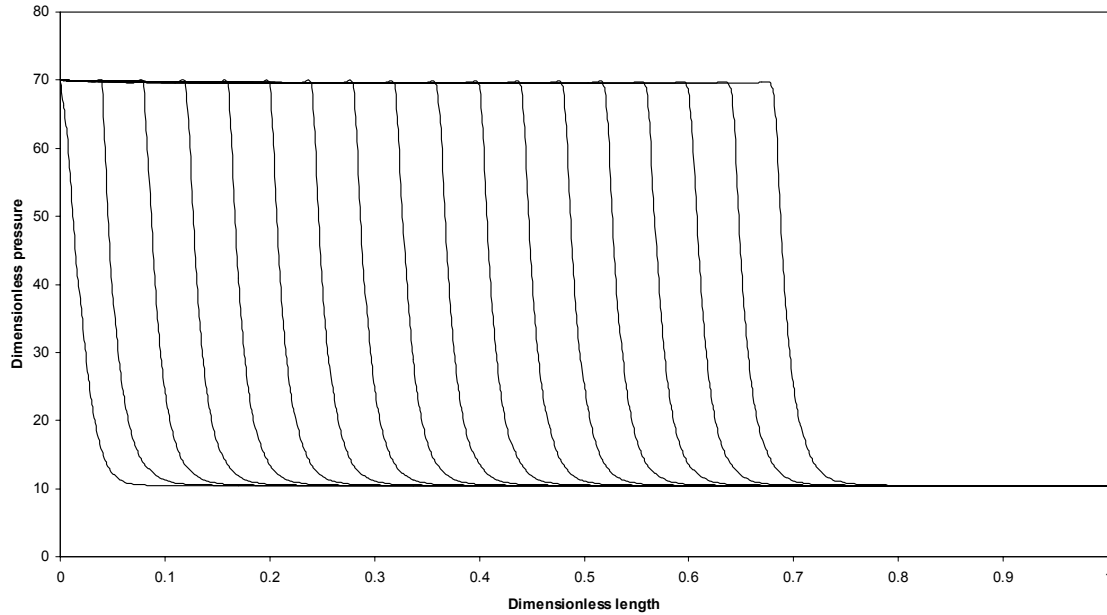


Figure 48. Dimensionless pressure profile with $\Delta\tau = 0.004$.

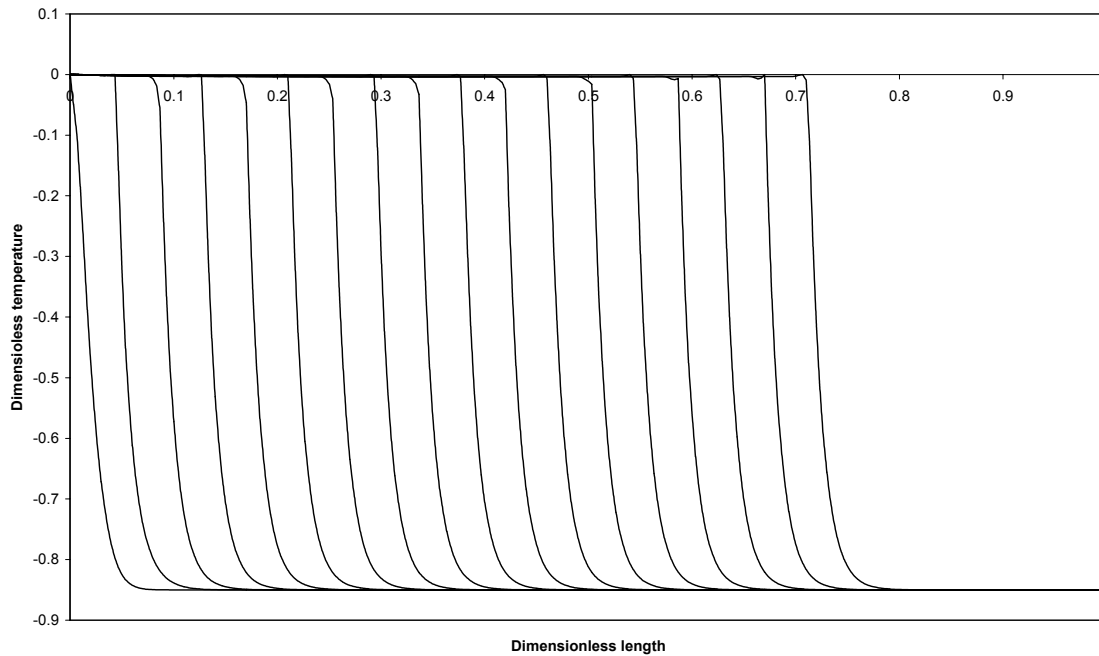


Figure 49. Dimensionless temperature profile for 70 bars (1000 psi) with $\Delta\tau = 0.004$.

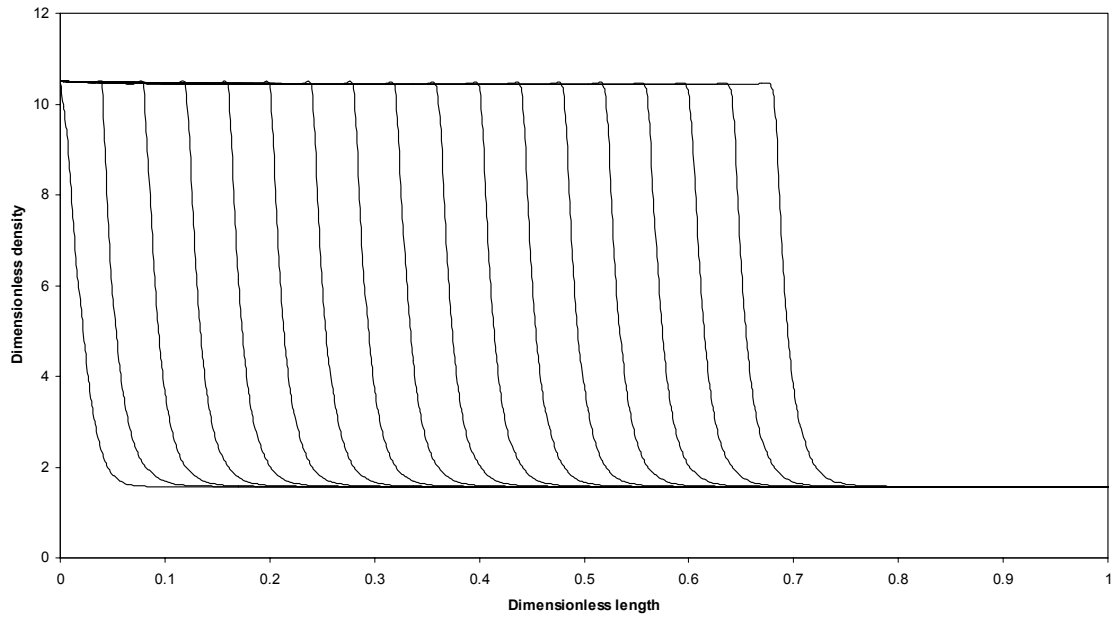


Figure 50. Dimensionless density for 70 bars (1000 psi) with $\Delta\tau = 0.004$.

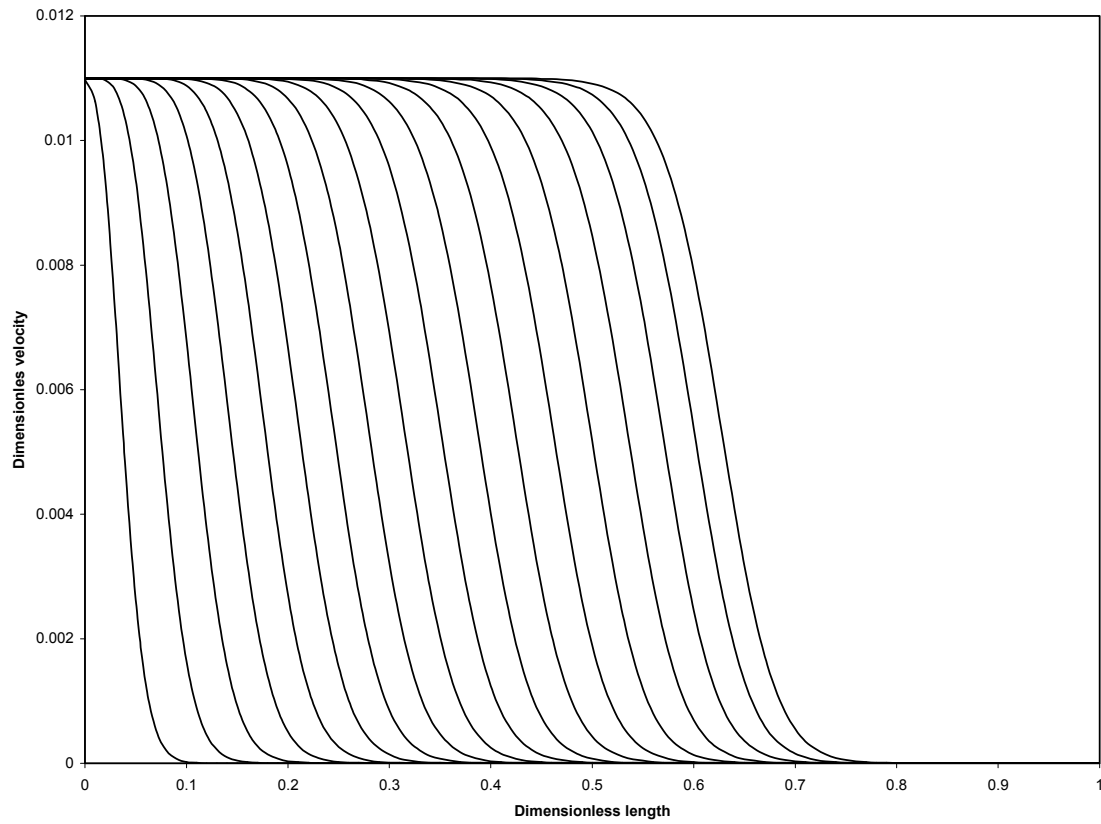


Figure 51. Dimensionless velocity profile for 70 bars (1000 psi) pressure with $\Delta\tau = 0.004$.

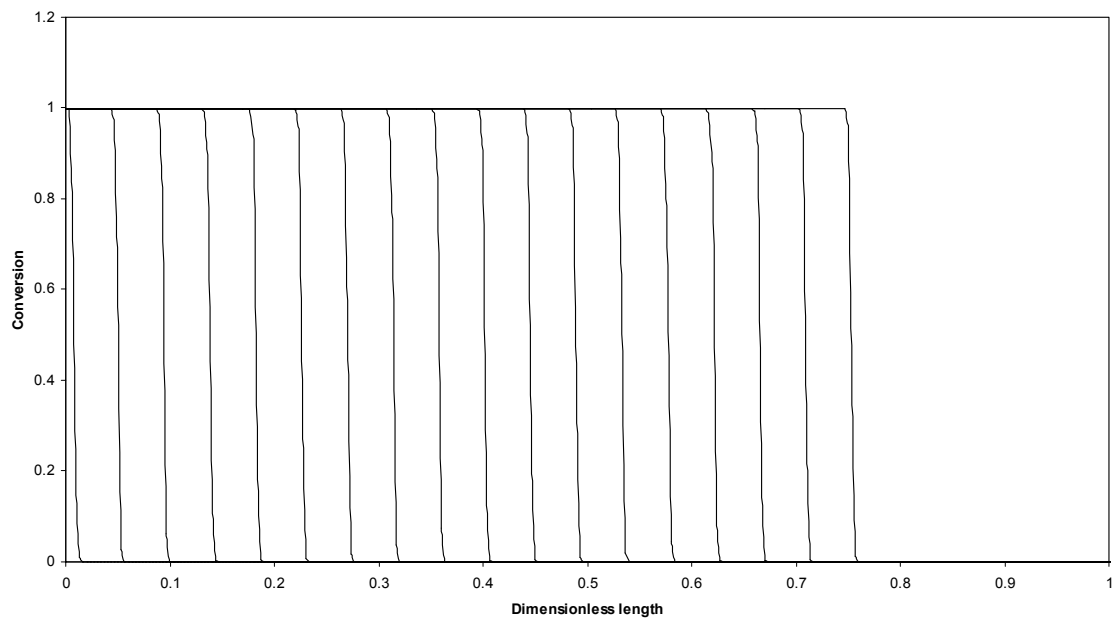


Figure 52. Conversion profile for pressure 70 bars (1000 psi) with $\Delta\tau = 0.004$.

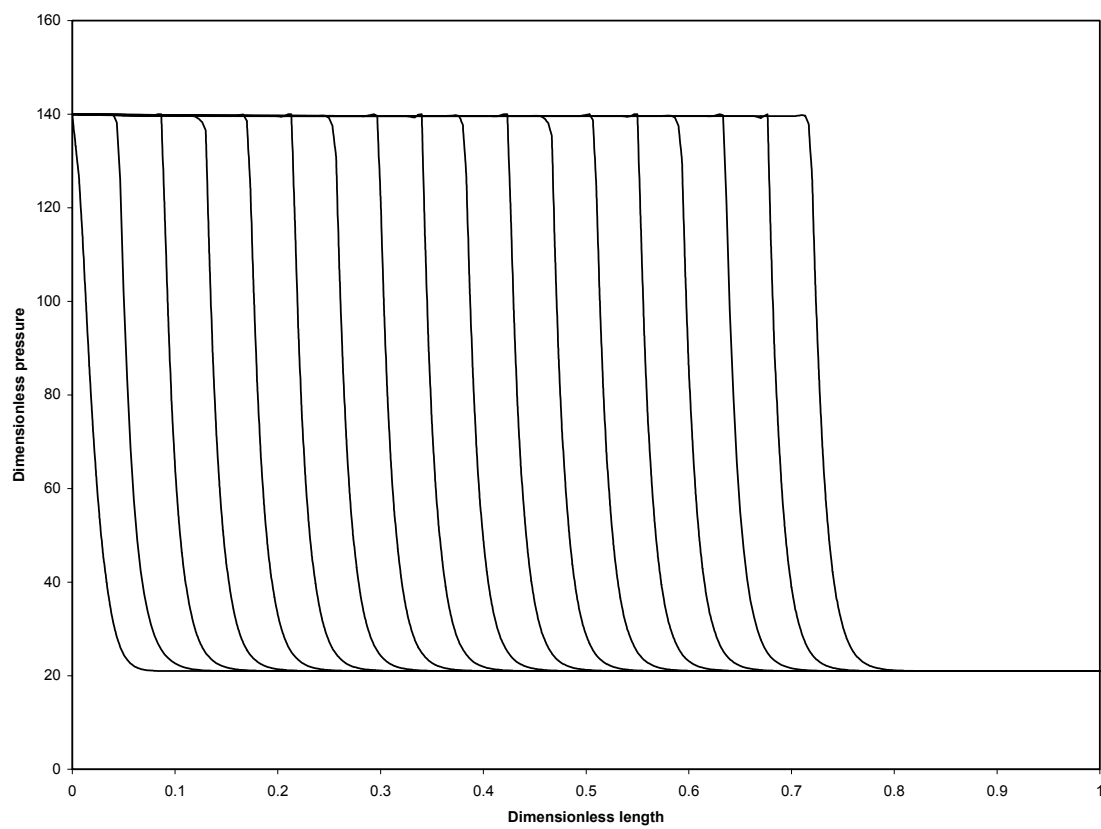


Figure 53. Dimensionless pressure profile with $\Delta\tau = 0.003$.

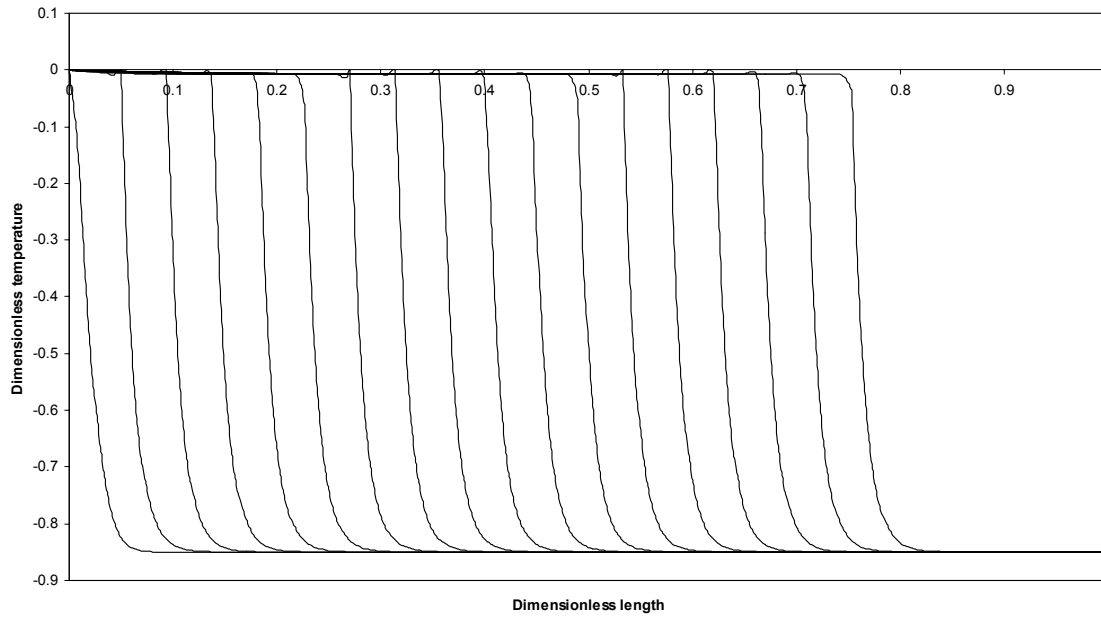


Figure 54. Dimensionless temperature profile for 2000 psi pressure with $\Delta\tau = 0.003$.

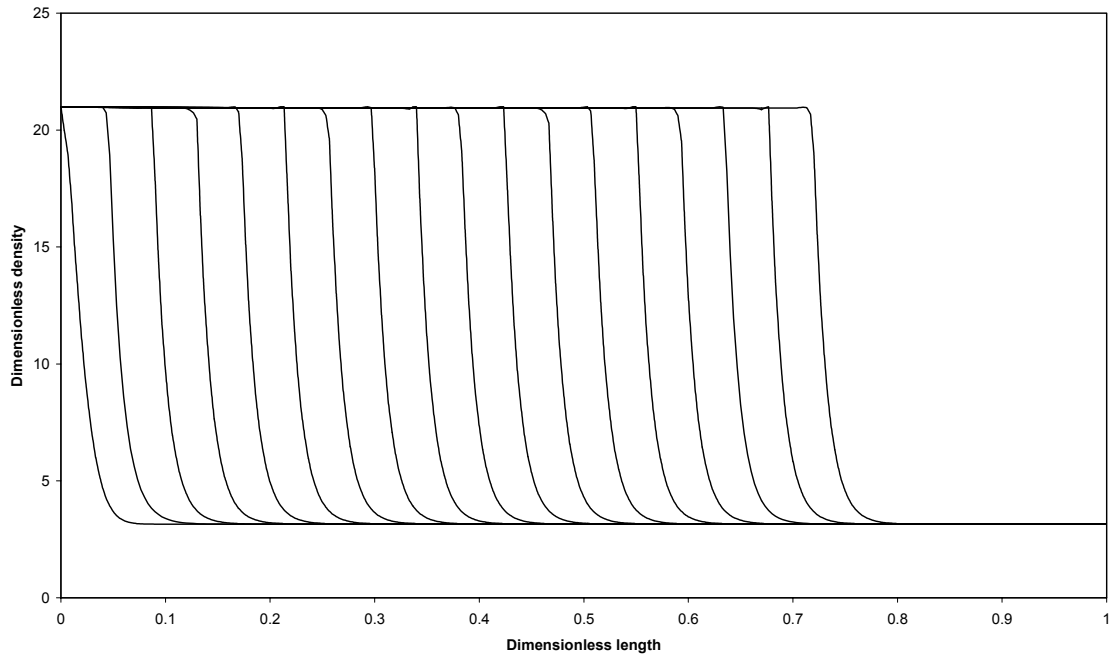


Figure 55. Dimensionless density profile for 2000 psi pressure with $\Delta\tau = 0.003$.

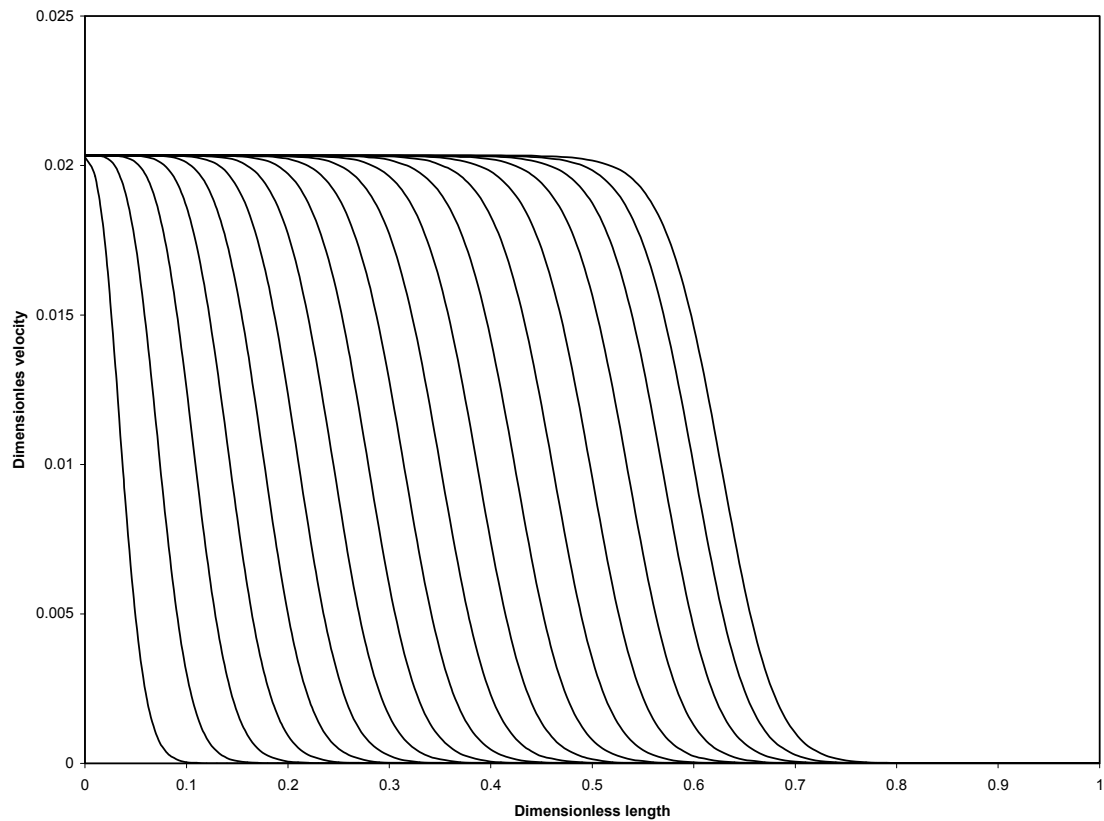


Figure 56. Dimensionless velocity profile for 2000 psi pressure with $\Delta\tau = 0.003$.

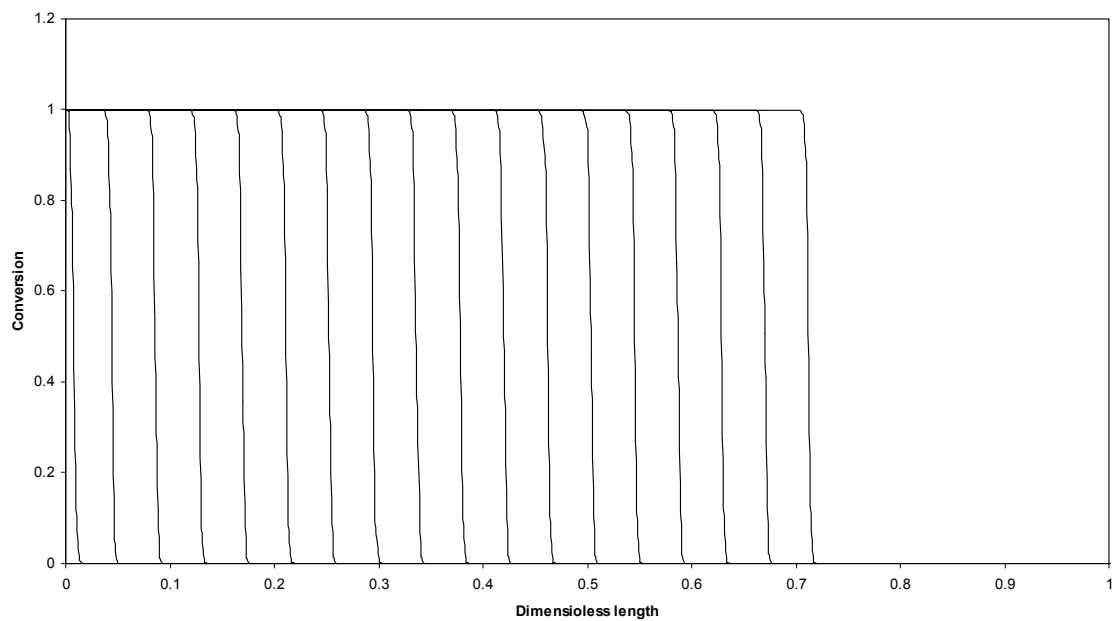


Figure 57. Conversion profile for 2000 psi pressure with $\Delta\tau = 0.003$.

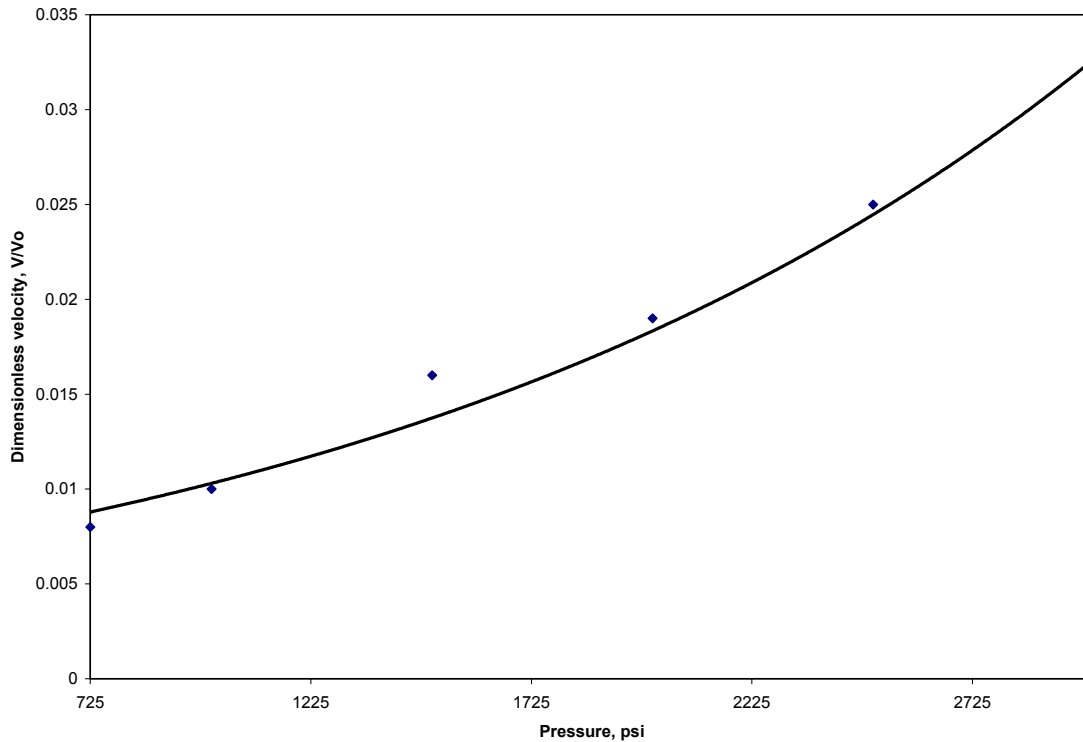


Figure 58. Dimensionless velocity profile at various pressures.

As can be seen from Fig.35, as the pressure is increased from 725 psi to 3000 psi the dimensionless velocity increases from 0.008 to 0.03 and the propagation become much faster. However, further investigation on other parameters is necessary to understand this system.

BIBLIOGRAPHY

1. Grimblot, J., and Eldridge, J. M., "Influence of the Growth Conditions of Al_2O_3 Passivating Layers on the Corrosion of Aluminum Films in Water". *Journal of the Electrochemical Society*, 1981, 128, 4, 729-731.
2. Deepak Shivaprasad *Combustion Characteristics of Ti-Mo-Si Reacting Systems* [M.S Thesis], SDSM&T, 2000.
3. A. Varma, A.S. Rogachev, A.S. Mukasyan, and S. Hwang; *Combustion Synthesis of Advanced Materials Principles and Application*, Department of Chemical Engineering, University of Notre Dame, Notre Dame, Indiana, p 124-25.
4. Oran S. E. and Boris P.J *Numerical Simulation of Reactive Flow*, 1987 Elsevier.
5. A.G. Merzhanov, E.N. Rumanov, and B.I. Khaikin, "Multizone Combustion of Condensed Systems," *Prikl. Mekh. Tekh. Fiz.*, No. 6, 99-105 (1972).

6. B.V. Novozhilov, “*The Velocity of Propagation of the Front of an Exothermic Reaction in the Condensed Phase*,” Dokl. Akad. Nauk SSSR, 141, 151-154 (1961).
7. E.I. Maksimov, and A.G. Merzhanov, “*On the Theory of Combustion of Condensed Substances*,” Fiz. Goreniya Vzryva, 2, No.1, 47-58 (1966).
8. Yogesh Jaluria, Kenneth E. Torrence, *Computational Heat Transfer*, 1986, New York.
9. Bird, R.B., Stewart, E.W., and Lightfoot, N.E., *Transport Phenomena*, 1994, John Wiley and Sons.
10. H.S. Fogler, *Elements of Chemical Engineering*, 3rd ed. (1999), Prentice Hall.

PUBLICATIONS, PRESENTATIONS, AND TECHNICAL REPORTS

The following presentations and publications resulted from this research:

PRESENTATIONS

1. J.A. Puszynski, B. Liebig, T. Kerr and S. Valliappan, “Characterization and Reactivity of Aluminum Nanopowders” 2002 Annual AIChE Meeting, Indianapolis, IN November 3-8, 2002.
2. J.A. Puszynski, J. Swiatkiewicz, S. Valliappan, and T. Kerr, “Challenges in Processing and Characterization of Energetic Materials”, 2003 Nano Materials for Aerospace Symposium, Corpus Christi, TX, 27-30 January, 2003.
4. S. Valliappan, C. Bulian and J. A. Puszynski, “Investigation of Al-CuO Nanocomposite Reacting System”, 30th International Pyrotechnics Seminar, EuroPyro 2003, Saint Malo, France, June 23-27, 2003.
5. J.A. Puszynski, “Reactivity of Nanosize Aluminum with Metal Oxides and Water Vapor”, 2003 Fall MRS Meeting, Boston, MA, December 1-4, 2003.
6. S. Valliappan, T. Kerr, S. Swiatkiewicz, and J.A. Puszynski, “Reactivity of Aluminum Nanopowders with Metal Oxides”, 2003 Annual AIChE Meeting, San Francisco, CA, November 16-21, 2003.
7. S. Valliappan and J.A. Puszynski, “Combustion Characteristics of Metal-Based Nanoenergetic Systems”, S.D. Academy of Science Conference, Rapid City, SD, April 2003.

PUBLICATIONS

1. Bulian, C.J., Kerr, T.T., and Puszynski, J.A.; “**Ignition Studies of Aluminum and Metal Oxide Nanopowders**”, accepted for publication in 31th Proceedings of the International Pyrotechnic Seminar, (2004).

2. Puszynski, J.A., **“Recent Advances and Initiatives in the Field of Nanotechnology”**, **(invited)**, accepted for publication in 31th Proceedings of the International Pyrotechnic Seminar, (2004).
3. Puszynski, J.A.; **“Reactivity of Nanosize Aluminum with Metal Oxides and Water Vapor”**, accepted for publication in 2003 MRS Proceedings, (2003).
4. Valliappan, S., Swiatkiewicz, S., and Puszynski, J.A.; **“Reactivity of Aluminum Nanopowders with Metal Oxides”**, submitted to Journal of Powder Technology, (2004).
5. Valliappan, S. and Puszynski, J.A.; **Combustion Characteristics of Metal-Based Nanoenergetic Systems”**, Proceedings of S.D. Academy of Science, Vol 82, 97-101, (2003).
6. Valliappan, S., Bulian, C., and Puszynski, J.A., **“Investigation of Al-CuO Nanocomposite Reacting System”**, Proceedings of EUROPYRO 2003, Vol. 2, 536-541, 2003.

PARTICIPATING PERSONNEL

Dr. Puszynski supervised and coordinated entire research project.

The following graduate and undergraduate students participated in that research:

Berthold Liebig, Ph.D Materials Engineering and Science; Somu Valliappan, M.S. Chemical Engineering; Gatwech Thich, M.S. Chemical Engineering; Shivanee Dargar, M.S. Materials Engineering and Science; Amit Kurupathi, M.S. Materials Engineering and Science; Chris Bulian, M.S. Chemical Engineering; Sara Farber, undergraduate ChE student; Sarwat Hassan, undergraduate ChE student.

In addition, Dr. Swiatkiewicz assisted students with all characterization methods.

REPORT OF INVENTIONS

No inventions were made during this one year research grant.